DEVELOPMENT OF CFD SIMULATION FRAMEWORKS FOR HIGH FIDELITY PREDICTIONS OF QUADCOPTER AERODYNAMICS

by

Karthik Srinivas Madabushi

A thesis submitted to the faculty of
The University of North Carolina at Charlotte
in partial fulfillment of the requirements
for the degree of Master of Science in
Mechanical Engineering

Charlotte

2020

Approved by:

_____

Dr. Mesbah Uddin

_____

Dr. Jun Xu

_____

Dr. Amirhossein Ghasemi

ABSTRACT

KARTHIK SRINIVAS MADABUSHI, Development of CFD Simulation Frameworks for High Fidelity Predictions of Quadcopter Aerodynamics.
(Under the direction of DR. MESBAH UDDIN)

External aerodynamic simulation of a rotor system is far more challenging compared to simulations involving fixed wing aircraft. This is because the surrounding flow field itself is far more complex. The rotating blades of the rotor system encounters its tip vortex and as well as the tip vortices of other blade in a phenomenon known as Blade Vortex Interaction (BVI). These complexities make the modeling of a rotor system and accurate predictions of rotorcraft performance challenging. Rotary wing Micro Aerial Vehicles (MAV) are such systems that have unique capabilities of vertical takeoff and lift (VTOL), hover, and low-speed flight. Quadcopters are such rotary-wing MAV that involve multi-rotor systems. Given that the modeling of a single rotor system is complex, modeling of a system with multiple rotors is even more challenging due to the rotor - rotor and rotor - fuselage interactions. This thesis explores and evaluates the computational modeling of a commercial quadcopter in hover using Computational Fluid Dynamics (CFD) simulations. A high fidelity CFD simulation methodology is first developed for an isolated rotor through investigating the effects of various simulation parameters like meshing schemes, turbulence modeling, and flow-physics setups on the veracity of the CFD predictions. Rotorcraft performance parameters such as the thrust coefficient, torque coefficient, Figure of Merit, and blade surface pressure coefficients are validated against and correlated to experimental data obtained using the Caradonna and Tung rotor. Proper resolution of the rotor wake region to prevent any grid related dissipation is observed to be critical for a reliable CFD simulation. This simulation methodology is further validated by comparing CFD simulations of an isolated rotor of the quadcopter (DJI Phantom- 3) car-

ried out against available experimental results. This double verification approach enables the developing and testing of a CFD methodology for rotorcraft flow-field simulations. Unsteady Reynolds-Averaged Navier-Stokes (URANS) and Improved Delayed Detached Eddy Simulation (IDDES) models are used in the case of DJI Phantom-3 quadcopter to predict its performance and of its individual components. Limitations of URANS in accurate prediction of rotor-rotor and rotor-fuselage interactions are studied. Differences in predictions of commercial CFD code StarCCM+ against OVERFLOW code is studied for quadcopter applications.

ACKNOWLEDGEMENTS

I would like to express my sincere gratitude to my advisor Dr. Mesbah Uddin first for giving me the freedom to work on a research topic that I am interested in. He not only advised me on how to proceed with the research but also overlooked and helped me grow professionally and personally. I would also like to thank Dr. Jun Xu and Dr. Amirhossein Ghasemi for providing their valuable insights into my research and being part of my thesis committee. All my colleagues at NC MARC especially, Sridhar Dangeti, Hamed Ahani, Shadab Anwar, and Adit Misar have played a pivotal part during my time at UNCC. The continuous efforts of the Department of Mechanical Engineering to have a smooth journey at UNCC are unforgettable. A very big kudos to UNC Charlotte High-Performance Group for their vigilance and ready availability. A special thanks to Jon Halter for being there for any issues with the cluster. The impact Dr.Bruce Webster had on my research and my understanding cannot be undermined and a special salutation to him.

DEDICATION

Dedicated to the future it beholds.

TABLE OF CONTENTS

LIST OF TABLES

LIST OF FIGURES

CHAPTER 1: INTRODUCTION

Unmanned Aerial vehicles(UAV), drones, quadcopters, or other Micro Aerial Vehicles(MAV) have risen to prominence over the last decade. Application of these MAV ranges from civil, military, photography, agriculture to surveillance, etc. Design of these vehicles is generally based on an approach "sketch, build, fly and iterate". This approach although is successful till now, there is no clear pathway to determine the next logical steps for design improvements. Initial designs of these rotary-wing aircraft are based on design concepts of large helicopters. But with the ever increasing demand for these vehicles, it is necessary to optimize the design and make it efficient. This would help increase the flight time, control, safety, and even range of operation.

Rotary wing MAV's are a special class of these vehicles with unique abilities of hover, low-speed flight, and vertical takeoff and lift(VTOL). Aerodynamics of a rotary-wing is complex and differs from that of a fixed wing. A blade when rotating sheds vortex structures from its tip and eventually encounters either its shed vortex or that of another blade. This phenomenon is known as Blade Vortex Interaction (BVI). These interactions between rotating blades and their wake systems have a significant effect on the performance prediction. The flow associated with a rotor system is unsteady, non-linear, and very hard to model. Constantly changing aerodynamic environment and loads is a characteristic of rotorcraft flow. Given that modeling of a single rotor system is complex, modeling of a system with multiple rotors is even more challenging due to rotor-rotor and rotor-fuselage interactions. In a quadcopter, a rotating blade is influenced by the interactions of its rotor system and also due to the presence of rotors and fuselage in close vicinity.

Low fidelity tools can be a good way to predict the performance of a single rotor system and may predict the performance of MAV with reasonable accuracy. It is not possible for these tools to account and quantify these rotor - rotor and rotor - fuselage interactions. In recent years there has been tremen-

dous growth in the computational power available and also parallelization of the workflow enabled researchers to simulate complex flows using high fidelity CFD techniques. These high fidelity CFD methods can also be used to calibrate low fidelity methods to improve their accuracy. Accurate depiction of the flow field phenomena, vortex structures, and wake geometry is also made possible with these methods. With these favorable conditions, CFD has emerged as an analytical tool to make headway in rotorcraft research.

Much of the earlier research conducted in the field of rotorcraft was for helicopter rotor applications or marine propeller applications. Although these applications are part of rotorcraft, these operate in a very different conditions and Reynolds number. The traditional design philosophies based on helicopter rotors may not apply to MAV rotors which operate at a very low Reynolds number regime of about 10,000 - 50,000. This has led to renewed interest in research into low Reynolds number regime flow for rotorcraft.

The desire to improve the performance of a quadcopter either by increasing thrust produced by rotors or by reducing the interactions between them needs to be explored. The efficiency can also be improved by using a sleek design for fuselage by reducing drag during forward flight conditions. Directly working on the entire model would be computationally expensive and time consuming. To avoid this, flow around simplified rotor system which requires similar numerical and flow modeling has gained importance and is considered as primary validation point. These simplified rotor systems are modeled and the obtained numerical results are validated against experimental data.

1.1 Motivation

Computational Fluid Dynamics(CFD) of isolated rotor systems of helicopters, propellers, and ducted fans have been extensively studied in the literature. In spite of this extensive literature available the flow associated with a MAV rotor is of low Reynolds number regime. The earlier research which was performed

at high Re cannot be directly implemented for these micro rotors. At such low Re, the flow around an airfoil has two immediate effects. First, due to strong viscosity effects of the flow the ability to withstand adverse pressure gradients is decreased which may lead to separation. This also causes a decrease in maximum lift produced and pressure drag increase. Second, there is an increase in skin friction drag if the flow is not separated. Based on the extensive literature available for isolated rotor systems computational models are developed for micro rotors and a quadcopter model. This research aims to produce a CFD methodology required to accurately predict the aerodynamic parameters of a quadcopter vehicle. In this article Unsteady Reynolds-Averaged Navier-Stokes (URANS)/ Improved Delayed Detached Eddy Simulation (IDDES) models are used and their extent of accuracy is compared with DDES models, hybrid turbulence modeling.

The quadcopter system involves rotor - rotor and rotor - fuselage interactions which are detrimental in determining the aerodynamics. In forward flight conditions the wake of front rotors of quadcopter effect the aft rotors performance. The aft rotors operate in disturbed wake flow from the front rotors and have a decreased performance due to this. Studies show that the fuselage acts as a wall and helps in improving the performance of a rotor and also reduces the rotor - rotor interactions. These interactions are not present in the case of an isolated rotor system. This study also tries to address these questions and help in quantifying them.

1.2 Outline of the Thesis

This thesis aims to develop a framework for CFD simulations of rotorcraft in hovering conditions. High fidelity schemes are developed as part of this research and their veracity is validated against the available experimental data[27]. In order to develop this methodology for a multi-rotor system like quadcopter which constitutes multiple rotor-rotor interactions and rotor-

fuselage interactions, first CFD methodology is developed for a simple rotor system of Caradonna and Tung rotor. After primary validation of this simple rotor system, the CFD methodology developed is applied for an isolated rotor system of the quadcopter. The performance of this methodology for quadcopter prediction is presented in the last part of this thesis.

1.3 Goals

There have been many CFD simulations performed by various authors for predicting performance of a quadcopter. Most of the research performed is aimed for steady state results as per author's knowledge. This research differentiates from those in various aspects and the highlights of this research are mentioned below.

- High fidelity simulations are performed for quadcopter and rotor systems and emphasis is placed on studying the wake of these rotor systems.
- Developing a framework for studying the performance prediction of any rotor system in general is established in this thesis.
- Exploring the aspect of URANS modeling for multi-rotor system predictions and identifying its limitations when compared to other models like IDDES.
- Visualization of the wake for a DJI Phantom 3 quadcopter and the performance of its individual components in hovering conditions.

1.4 Organization of Thesis

The thesis is organized in the following manner: Chapter 1: Provides an introduction to the concept of this research, the motivation behind it, and an outline of the rest of the document.

Chapter 2: Summarizes the literature review conducted and background for this research.

Chapter 3: Description of turbulence modeling used in this research.

Chapter 4: Elucidation of numerical setup, methodology, simulation parameters, and boundary conditions.

Chapter 5: Results and discussions of various simulations along with grid, time step independence studies.

Chapter 6: Concludes this research and provides the scope of further research.

CHAPTER 2: BACKGROUND

A rotor undergoes a wide variety of flight conditions like hover, cruise, or maneuvering. Aerodynamics of each flight condition is different and has different effect on the performance. While cruising and hovering are more efficient, maneuvering requires high performance. Hovering condition of a rotor remains as the true limiting point in terms of design[1]. Accurate numerical modeling of a rotor in hover requires precise prediction of aerodynamic parameters and also vortex wake. For a fixed wing in forward flight, the tip vortex shed and vortex sheet generated are quickly convected away into the far field and far away from the body. For modeling such phenomenon, it is sufficient to capture the initial tip vortex near the wing. Due to the convection of these vortices into the far field their influence on the aerodynamics of wing is negligible. We can see the vortex line and tip vortex flow for a fixed wing aircraft in the figure 2.1. It is entirely different for the case of a rotor system. The tip vortices loiter in the neighborhood of the rotating wing and form a helical sheet beneath. These exert significant influence on the aerodynamics of the blade and alter the flowfield. The effective angle of attack is changed due to the presence of these dominant flowfield structures. Figure 2.2 shows a schematic of tip vortices and vortex sheet of a rotor in hover.

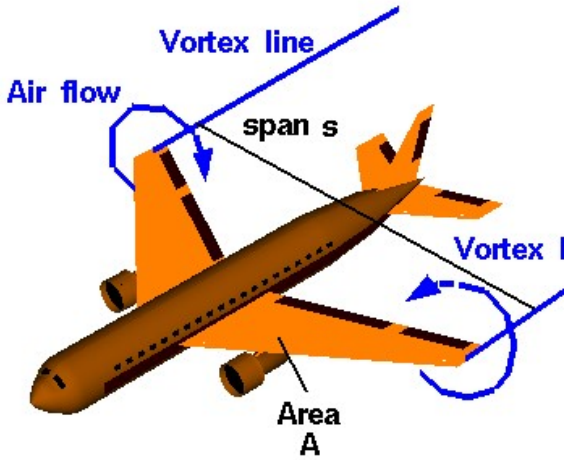

Figure 2.1: Vortex structures of a fixed wing aircraft[2].

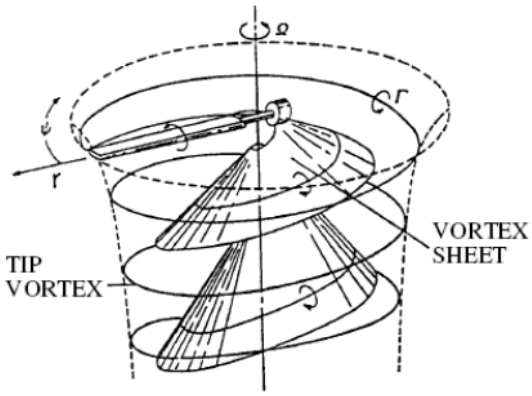

Figure 2.2: Vortex structures of a rotor blade [3].

Earlier modeling of the hovering rotor systems was done using theories like Prandtl's lifting line theory and blade momentum theory. These theories proved to be sufficient for the initial design and development at that time. Numerical simulations performed applied Euler methods excluding the effects of viscosity or full potential equations to solve for the flowfield. Computational power available at that time was not even enough to conserve the tip vortices from diffusing due to grid related dissipation[4]. Higher-order methods are also a way to convect the tip vortices generated with greater accuracy but these also require a minimum grid requirement to be satisfied.

Any literature tackling the problem of hovering rotor follows a certain mesh methodology that concentrates on two areas. First, the near field region which encompasses the near wake and boundary layer is modeled. Body fitted grids are generated for the wings of a rotor in the near field region. These body fitted grids move along with blades. Most of the applications tackling this problem use the overset mesh method. Overset mesh helps us in refining the mesh near the rotating wing as required. The other advantage of this method is it helps in reducing overall computational requirements. Second is the way how we treat the rotor wake region. Cartesian grids are used for resolving the wake region and these grids encompass the near body grids. Care needs to be taken at the junction of the near body grids and cartesian grids for efficient transfer of information. The boundaries of these two regions need to

be of similar resolution, aspect ratio, skewness, and clustering. The location of the overlapping cells should also be far away from high gradient regions[5]. Strawn, R. C., et al[6] have developed a modeling scheme for UH-60A rotor where two cell overlap is used instead of one cell overlap. Using two cell overlap ensures continuity in the transfer of flowfield information along with flowfield derivative information. There is no loss in the spatial accuracy over the whole domain when two cell overlap is used.

Periodicity is used for most of the isolated hovering rotor calculations with periodic boundary conditions. Periodicity is not used in this research as the original intent of this thesis is to develop a consistent meshing methodology for commercial grade quadcopters and their isolated rotor systems. Periodicity can be used to decrease the computational requirements by a factor of n, where n is the number of the blades. The boundary conditions opted for the numerical simulations must satisfy two criteria. First, boundary conditions must represent the physical phenomena reasonably. Second, they should be compatible with characteristic wave propagation theory for N-S equations.

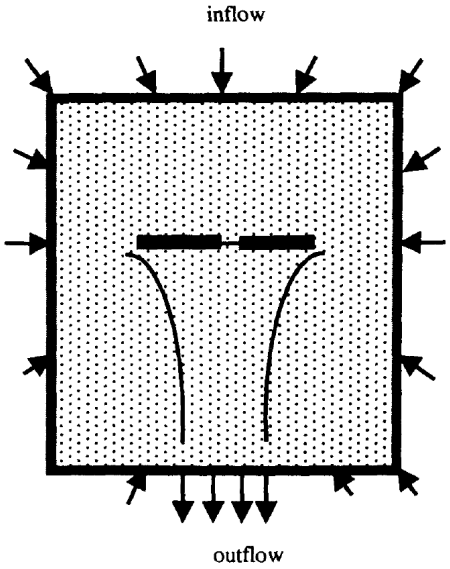

Figure 2.3: Souce - sink boundary condition for rotor in hover [4].

Ideal boundary conditions are selected and tested in the further section to represent hover phenomena. Source - sink condition is such ideal boundary

conditions which represents the flow in the rotor phenomena. Rotor is a type of propeller or ducted fan which pulls in air from upstream and pushes it further downstream generating forces. This can be visualized in the above figure where the rotor hub center acts as a sink and the boundaries are sources. The strength of the sink in these simulations is adjusted in such a way that mass is conserved in the domain. These boundary conditions also facilitate smaller computational domain requirements than otherwise would be required in case of zero velocity conditions at the boundary.

2.1 Caradonna and Tung rotor

Development of numerical codes and assessment of their performance needs a reference to be validated against. Experimental studies performed by Caradonna and tung is a benchmark towards achieving this goal. Rotor performance data including blade surface pressure coefficients, sectional thrust coefficients, lift values for a wide range of rotor speeds across the subsonic to transonic regime has been made available. The experimental setup used in this study is described below in the figure 2.3. Two rectangular cantilever blades are used as the rotor wings with a profile shape of NACA 0012. The blades used in this experiment are untwisted, untapered with an aspect ratio of 6. The blades are manufactured in such a way that it can accommodate pressure sensors in the grooves. These pressure sensors are located at 5 different radial locations to get an estimate of sectional pressure coefficients. Both blades are embedded with pressure sensors at a radial location of 0.8 to check the symmetry in loadings. This experiment is used in the further studies for verification of our CFD methodology. The vortex structures produced in this experiment closely resemble a classical Rankine vortex and become non classical at higher speeds.

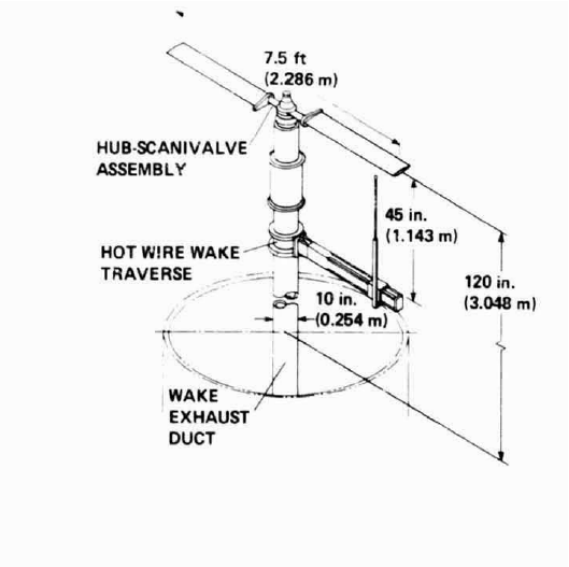

Figure 2.4: Caradonna and Tung rotor experimental setup [7].

The above experimental setup has most of the geometrical features clearly indicated. Detailed information on some important features like rotor hub geometry, blade tip shape, and trailing edge is not provided. Some assumptions are made with respect to the geometry. Root cut radius is assumed to be 0.25 times radius, Sharp trailing edge is considered and flat tip surfaces are selected[3].

Ahmad, J. U., et al[8] have computed the performance of Hovering rotor and wake using an Overset-Grid Navier Stokes solver. High-resolution grids are used in the near field region of the blade and accompanied by the systematic increment in grid resolution in the rotor wake region. Experimental measurements made by Caradonna and Tung earlier are now compared to the computational results obtained. Grid independence is also studied here by varying the resolution in the wake region keeping the near field same.

Accuracy of hover simulations requires precise predictions of the following. Integrated performance numbers or integrated quantities like thrust, lift or drag and radial surface pressure distributions are the parameters that would determine the accuracy of the hovering rotor model[1]. In the further chapters, we develop modeling techniques in order to achieve this.

2.2 Isolated Phantom rotor

Caradonna and Tung rotor provides a fundamental understanding of the modeling of rotors in hover. The micro rotors which are representative of the isolated rotors of small-scale MAV's operate in an entirely different regime than that of Caradonna and tung rotor[13]. The characteristic length of the rotor system is its own chord length. The chord length of a MAV rotor is low(0.01) and is about 2 orders less than that of Caradonna and Tung rotor (1m).

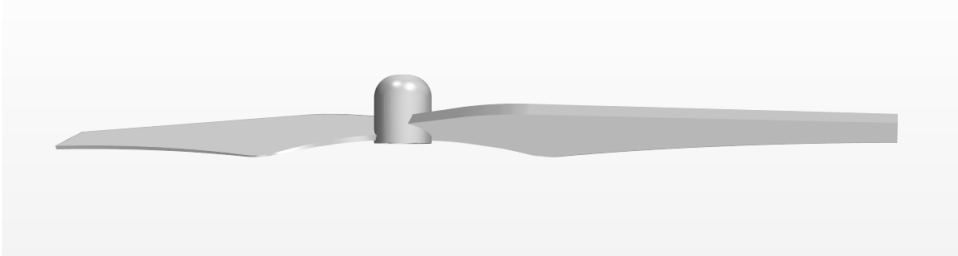

Figure 2.5: Isolated phantom rotor.

The modeling schemes used for CT rotor would act as a good starting point to work on for other rotors. The near field modeling and far field modeling which we emphasized earlier is tweaked to suit isolated micro-rotor. Zawodny, N. S., et al[9] also developed a CFD approach for isolated phantom rotor based on the success of CFD for helicopter rotor blade. This solidifies the intent of this thesis of first proceeding with validation of CT rotor and building CFD model of isolated MAV rotor based on it. S-A turbulence model is used in this article along with similar near and far field regions through the use of chimera and cartesian grids.

The results for thrust coefficient with increasing RPM levels show a slight increase and is almost a horizontal line. Whereas the trend for thrust with RPM as shown in the figure below shows a linear increase with RPM. This is as expected as the rotor when operating at higher speeds produces more thrust. SALT experiment is an experiment conducted to study the noise levels and other acoustic characteristics for various isolated rotor configurations. DJI phantom rotor is one of these which have been studied in this experiment and

hover performance is also measured.

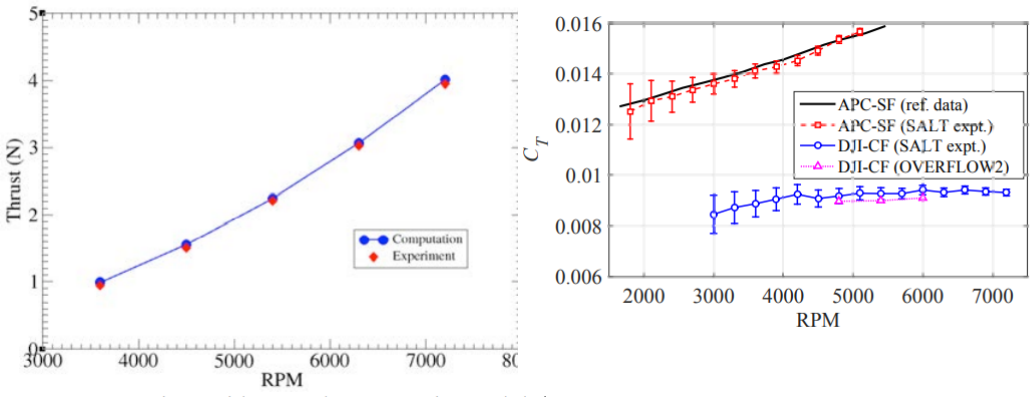

Figure 2.6: Isolated Phantom rotor hover performance (a) Thrust vs RPM[10] (b) Thrust coeff vs RPM [9].

Modified phantom rotor with a narrow gap between hub and blades is also used to study the effects of collectives on the performance. The gap is introduced to allow modifications to the collective pitch settings and is made small so as to prevent its effect on flow characteristics. The gap is carefully designed to allow a change in collective pitch up to 20 deg. A systematic study has been performed with varying pitch results and an interesting outcome has been observed. A higher pitch setting at a lower RPM is found to generate thrust equal to a higher RPM at a lower pitch setting[10]. In the figure 2.7 we can observe with increasing collective angle large regions colored in red are formed. These red-colored regions indicate high downwash speeds in downstream of the rotor which results in increased thrust production.

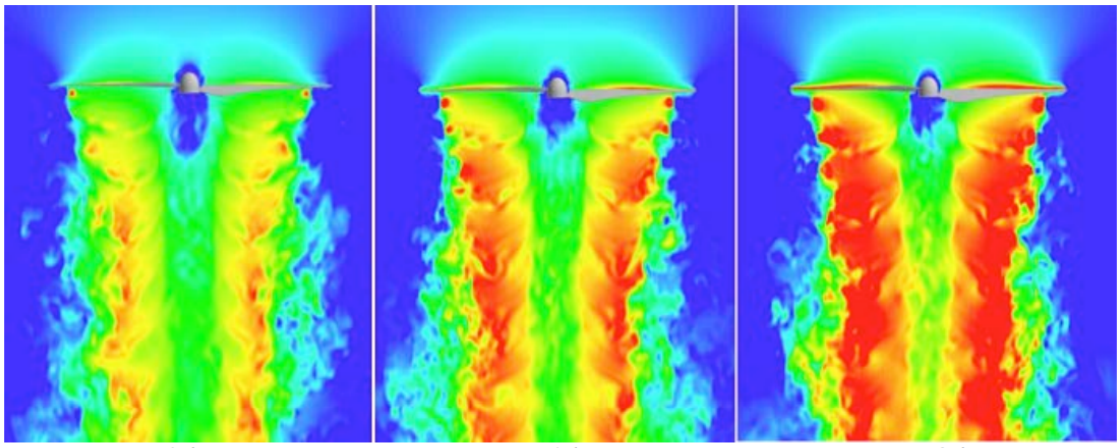

Figure 2.7: Velocity magnitude scenes of modified isolated phantom rotor at collective angles of 0,4 and 8 degree.[10]

2.3 DJI Phantom 3 Quadcopter

Multi-rotor configurations differ from isolated rotor configurations in various aspects. Rotor- rotor interactions is quite common for these multi-rotor configurations due to their close vicinity. Yoon, S., et al [11] studied the effect of inter rotor distance on the effect of their vertical force prediction. It has been observed that as rotor distance is increased to a distance of 2 times rotor radius, the performance reaches the value of an isolated rotor performance. The vertical thrust produced decreases as the distance is decreased between the rotors. The iso-surfaces of Q-criterion observed for multi-rotor configurations show that the rotor wakes are pulled towards the center. It also shows the ingestion of vortices from above the rotor into the wakes. The presence of fuselage helps in reducing these wake interactions as the fuselage functions as a blockade. The fuselage although produces download, it produces an overall positive effect by reducing the wake interactions.

Figure 2.8: DJI Phantom 3 Quadcopter[9]

The influence of the fuselage on a quadcopter vehicle is better understood through the study of three configurations researched in Yoon, S., et al [10]. Off body under-mount configuration with rotors on the underside produces less rotor thrust when compared to other configurations. This showcases the influence that the fuselage has on thrust production. Even though the fuselage download is lower for this case the total thrust produced is less. By placing the rotors with an offset on the underside of the body the presence of fuselage had no impact on rotor - rotor wake interactions. The under-mount configuration and over-mount configuration both produce almost the same amount of download on the fuselage. High downwash speeds are observed downstream of the rotor for over-mount configuration whereas it is found upstream of the rotor for under-mount configuration. There has been a slight decrease in the thrust produced for under-mount configuration which is representative of its inherent geometry.

Diaz, P. V., et al[12] has performed a study on simplified phantom quadcopter and original configuration. The landing gear and battery of DJI phantom is shown to produce download due to their presence in the wake flow. A reduction in thrust by about 1 percent is noticed due to these components. We can observe in the figure 2.9 that the battery and landing gear show red color which indicates high pressure and indicates being pushed down. Further analysis conducted in the paper shows that the presence of a camera and landing gear helps in mitigating pressure waves which reduces the noise levels produced.

Figure 2.9: Surface pressure coefficient of DJI phantom 3 when viewed from above[12].

CHAPTER 3: TURBULENCE MODELING

Most of the flows that we see in nature like smoke produced, the boundary layer of earth or fast flowing rivers are turbulent. Turbulence is not a fluid phenomenon rather it is a flow phenomena. It means that the dynamics of turbulence is not dependent on the type of fluid or its mechanical properties. As stated in H. Tennekes[23] it is hard to precisely define turbulence, but every turbulent flow has a certain set of characteristics. Turbulent flows are irregular, chaotic, and random. Due to this nature, it is treated using statistical methods instead of a deterministic approach. It is possible in the future to develop a full formal theory for turbulence instead of relying on statistical methods. Diffusivity of turbulence is one such key characteristic that is responsible for the transport of mass, momentum, and energy. Eddy diffusivity which will be described further is representative of this diffusivity. Reynolds number which is the ratio of inertial forces to viscous effects needs to be large for a turbulent flow. For a pipe flow this Reynolds number needs to be around 2000 for a transition from laminar to turbulent flow. A small disturbance created in the flow can trigger an early transition from laminar flow to turbulent flow. Rotationality or vorticity is always present in a turbulent flow. Turbulent flows are always three dimensional due to this vorticity.

Turbulence is an amalgamation of different length and time scales. The dissipative nature of turbulent flows means high energy containing large scales transfer the energy to small scales through a process known as energy cascade. The large scale motions extract the energy from the mean flow and help in providing the energy required for maintaining turbulence. In this process, energy transfer occurs through inertial and inviscid mechanisms to smaller structures. This process creates smaller and smaller structures till these reach a point where molecular diffusion is prominent. At this scale known as the Kolmogorov length scale, viscous dissipation of energy occurs. Richard Feynman stated that 'Turbulence is the most important unsolved problem of classical

physics' in 1970's and even with huge advancements in computational ability and mathematics it remains the same.

3.1 Turbulence Modeling

Fluid motion is governed by the Navier-Stokes equation. Navier-Stokes equation is a second-order partial differential equation with non-linearity. These equations express conservation of mass and momentum and are derived by applying Newton's second law to a fluid element. These equations have no closed analytical solution.

$$\frac{\partial u_i}{\partial x_i} = 0 \tag{3.1}$$

$$\frac{\partial u_i}{\partial t} + u_j \frac{\partial u_i}{\partial x_j} = \frac{-1}{\rho} \frac{\partial p}{\partial x_i} + \frac{\partial \tau_{ij}}{\partial x_j} \tag{3.2}$$

$$\tau_{ij} = \mu(\frac{\partial u_i}{\partial x_j} + \frac{\partial u_j}{\partial x_i}) \tag{3.3}$$

Equation 3.1 represents the conservation of mass equation while Equation 3.2 represents the conservation of momentum equation for incompressible and low Mach number flows. These equations are written in Einstein notation.

For a turbulent flow each quantity of these governing equations is decomposed into its mean and fluctuating part. These equations are ensemble-averaged as discussed in the earlier section that statistical methods are used for solving turbulence. Decomposing N-S equations and averaging give out RANS equations which also constitute non-linear terms. This is known as Reynolds decomposition and it creates more unknowns than equations available and this problem is popularly known as "The Closure Problem". Turbulence modeling is the aspect of constructing an additional set of required mathematic equations using reasonable and physically possible assumptions. These additional equations help in finding out numerical solutions to the RANS equations.

Figure 3.1 below gives us a brief idea of the resolving capability of different turbulence models that will be discussed further in this chapter.

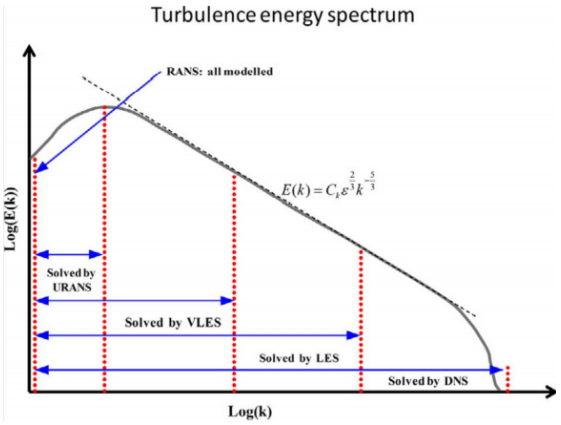

Figure 3.1: Turbulence energy spectrum[14]

3.2 Direct Numerical Simulations (DNS)

Navier-Stokes equations govern the motion of any viscous fluid. Direct Numerical Simulation (DNS) is a method in which these N-S equations are directly solved using various numerical methods. No turbulence modeling is required in this method as we are not working with RANS equations, instead N-S equations are directly tackled and resolved. In this method, all the scales of turbulence ranging from characteristic length scale (L) to the smallest dissipative scale i.e Kolmogorov length scale(ν) are resolved. Computational requirements for this method are highest and were practically unfeasible until the 1970s. The computational grid requirements of DNS scale with Reynolds number as follows($\propto Re^{9/4}$). Several DNS studies have been performed for wall bounded flows, flow past a cube, etc. Most of the DNS performed were for simple bodies and canonical flows at low to moderate Reynolds number. The computational resources available these days are not even sufficient to perform DNS for industrial applications. DNS is a fundamental research tool used by many researchers to get a crystal clear picture of the flow phenomena. DNS is also used as a validation tool for checking the accuracy of different turbulence models. Recently first ever DNS study for flow and heat transfer inside an internal combustion engine is performed at the US Department of Energy (DOE) Argonne National Laboratory. This simulation is computed

on 51,328 cores and required a solution of 2 billion degrees of freedom (DOF).

3.3 Large Eddy Simulations (LES)

LES is an approach mediocre between RANS and DNS and is motivated by their limitations. In DNS all the scales are resolved whereas in RANS all the scales are modeled. The high computational cost of DNS is expended near the smallest, dissipative scales of motion. Most of the energy in turbulence is present in the larger scale of motion[17]. So avoiding vast computational effort by modeling the smaller scales of motion and solving larger scales is the concept of the LES approach. As the large-scale motions are solved explicitly LES is assumed to have better accuracy when compared to RANS models for flows containing large-scale unsteadiness. Like the flows over a bluff body, involving vortex shedding and separations. The smaller scales are incorporated into N-S equations of filtered components in the form of a residual tensor known as SGS (Sub Grid Scale) stress tensor. The closure is obtained for LES by modeling this SGS tensor using eddy viscosity models and the accuracy of LES is dependent on it. There are also different variants of LES like Large Eddy Simulation with Near Wall Resolution (LES-NWR), Large Eddy Simulation with Near-Wall Modeling (LES- NWM), and Very Large Eddy Simulation (VLES). In LES, LES-NWR generally 80% of turbulent kinetic energy is filtered and explicitly solved with sufficient resolution near the walls. LES- NWM is a variant where the near wall area is modeled instead of explicitly solving as this requires a very fine grid near the wall rising computational cost. In the case of VLES, a substantial amount of energy is present in the residuals and this can be performed on coarser grids than LES.

3.4 Turbulent Viscosity Models

Reynolds decomposition of velocity gives out mean velocity field and fluctuating part, and ensemble averaging the N-S equations with the Reynolds

decomposition gives out Reynolds equations. These Reynolds equations along with Poisson equation or continuity equation defines the turbulent flowfield. Non-linear terms come up in the Reynolds equations as Reynolds stresses $< u_i u_j >$. Now there are 4 equations and a total of 10 unknowns with Reynolds stress tensor containing six independent unknowns. This closure problem involves determining an additional set of equations to model these unknowns. Equations 3.4 and 3.5 represents RANS equations in their incompressible form and presented in Einstein notation.

$$\frac{\partial U_i}{\partial x_i} = 0 \tag{3.4}$$

$$\frac{\partial U_i}{\partial t} + U_j \frac{\partial U_i}{\partial x_j} = -\frac{1}{\rho}\frac{\partial P}{\partial x_i} + \frac{\partial}{\partial x_j}(2\mu S_{ij} - \rho\overline{u_i{}' u_j{}'}) \tag{3.5}$$

Early models proposed to tackle this closure problem were simple but were inadequate in physical content and accuracy. Later on, models improved on these fronts but they no longer remained simple. Gradient diffusion hypothesis is such a simpler model attempted for the closure problem of turbulence. The turbulent viscosity hypothesis is also one such attempt introduced by Boussinesq in 1877. Reynolds stresses are modeled as shown in equation 3.6 as per this hypothesis and are seen to be dependent on turbulent kinetic energy k, eddy viscosity v_t, and mean strain tensor.

$$\overline{u_i' u_j'} = \frac{2}{3} k \delta_{ij} - \nu_t \left(\frac{\partial \overline{U_i}}{\partial x_j} + \frac{\partial \overline{U_j}}{\partial x_i}\right) = 0 \tag{3.6}$$

Different turbulence models differ in the way how they model this eddy viscosity. Mixing length models, algebraic models and Reynolds Stress Models (RSM) are such different modeling approaches to model Reynolds stress. Two equation models like $k - \epsilon$ model involve model transport equations that are solved for two turbulence quantities. The two quantities form a length scale, time scale, and also a viscosity quantity which completes the flow dependent

specifications and eliminates the requirement of any mixing length scales (l_m). In $k-\epsilon$ two-equation model, one transport equation is for turbulent kinetic energy k and another one for the rate of dissipation of turbulent kinetic energy ε. The model constants for these models are obtained from observing the model performance in canonical flows. The value of $C_\mu = 0.09$ is obtained when this model is applied for a simple turbulent shear flow. Jones and Launder have been credited for the initial development of this model[16]. Launder and Sharma have made significant improvements for the values of model constants. A well-known shortcoming of this model is its overprediction of the rate of spreading for the round jet but can be remedied by modifying model constants.

$k-\omega$ is also a two-equation model that solves for two turbulence quantities (k, ω) where ω is specific rate of dissipation. The choice of using ω as a variable has been first proposed by Kolmogorov. This model is found superior in its treatment of the viscous-near wall region and also to account for effects of streamwise pressure gradients. $k-\omega$ model is sensitive to free stream boundary conditions which is one of its limitations[19]. Menter proposed a two-equation model that combines the best of these two models. A blending function is used to switch between these two models. $k-\omega$ is used in the near-wall regions where $k-\epsilon$ tends to be inaccurate and it switches to $k-\epsilon$ when it reaches boundaries of the computational domain. The equations stated below represents the $k-\omega$ Shear Stress Transport(SST) model with model coefficients. Transport equations for the $k-\omega$ SST model is shown below[15].

$$\frac{\partial k}{\partial t} + U_j \frac{\partial k}{\partial x_j} = P - \beta^* k\omega + \frac{\partial}{\partial x_j}[(\nu + \sigma_k \nu_t)\frac{\partial k}{\partial x_j}] \tag{3.7}$$

$$\frac{\partial \omega}{\partial t} + U_j \frac{\partial \omega}{\partial x_j} = \frac{\gamma}{\nu_t} - \beta^* \omega^2 + \frac{\partial}{\partial x_j}[(\nu + \sigma_\omega \nu_t)\frac{\partial \Omega}{\partial x_j}] + 2(1 - F_1)\frac{\sigma_{w2}}{w}\frac{\partial k}{\partial x_j}\frac{\partial w}{\partial x_j} \tag{3.8}$$

$$P = \tau_{ij}\frac{\partial u_i}{\partial x_j} \tag{3.9}$$

$$\tau_{ij} = \mu_t(2S_{ij} - \frac{2}{3}\frac{\partial u_k}{\partial x_k}) - \frac{2}{3}\rho k \delta_{ij} \tag{3.10}$$

$$\mu_t = \frac{\rho a_1 k}{max(a_1\omega, \Omega F_2)} \tag{3.11}$$

If ϕ_1 represents any constant in the original $k-\omega$ model and ϕ_2 any constant in $k-\epsilon$ model . The coefficients for this model are calculated from blending function(F_1) from the equation 3.12.

$$\phi = F_1\phi_1 + (1 - F_1)\phi_2 \tag{3.12}$$

The coefficients for the set 1 (ϕ_1) are

$$\beta_1 = 0.0750, \sigma_{k1} = 0.85, \sigma_{w1} = 0.5, \kappa = 0.41, \gamma_1 = \frac{\beta_1}{\beta^*} - \sigma_{w1}\frac{\kappa^2}{\beta^*} \tag{3.13}$$

The coefficients for the set 2 (ϕ_2) are

$$\beta_2 = 0.0828, \sigma_{k2} = 1.0, \sigma_{w2} = 0.856, \kappa = 0.41, \gamma_2 = \frac{\beta_2}{\beta^*} - \sigma_{w2}\frac{\kappa^2}{\beta^*} \tag{3.14}$$

for both set 1 and set 2

$$\beta^* = 0.09, \alpha = 1 \tag{3.15}$$

Spallart-Allmaras model is a one equation model primarily developed for aerodynamic applications[18]. In this model, a single transport equation for turbulent eddy viscosity ν_T is accounted for. Although this model does not describe the turbulence like a two-equation model, it has proved to be successful for the aerodynamic flows over airfoils. As only one transport equation is solved along with RANS, the computational cost required is lesser than that for a two-equation model.

3.5 Detached Eddy Simulation(DES)

DES model is a hybrid approach of RANS and LES, where RANS is used in the boundary layer which reduces resources required and the LES model is used

outside the boundary layer. The large turbulent scales in these grids are grid resolved and the model switches to sub grid scale (SGS) formulation where the length scale is less than the grid dimension. In this approach, the turbulence length scale d is replaced by a $\overline{d}$ which is the minimum of distance from the wall and local grid spacing (Δ) times a coefficient C_{DES} as defined in equation 3.16.

$$\overline{d} = min(d, C_{DES}\Delta) \tag{3.16}$$

These changes can be understood in the following way, First, there is a reduction in the turbulence length scale. This approach also allows turbulence dissipation to remain active in the wake region as it is grid resolved because of LES activation. This does not also allow turbulent eddy viscosity to grow unchecked. This method helps in better prediction of torque coefficient and in turn the figure of Merit(FM) for rotor applications. Delayed Detached Eddy Simulation (DDES) is a variant where the RANS mode is effective in the entire boundary layer. DDES approach is used in the predictions of quadcopter and isolated quadcopter rotor for better predictions.

CHAPTER 4: NUMERICAL SETUP

This chapter elucidates numerical setup, mesh setup, and other simulation parameters that are used in this thesis. Most of the simulations that have been performed in this study are done in commercial CFD code STAR-CCM+ v13.04. The mesh setup is improvized over the course of this study to help realize better prediction results. Some of the settings are maintained similar throughout the study. A brief description of the models used and the reasons which support them is mentioned in this chapter. In this chapter, we first discuss the setup of the Caradonna and Tung (CT) rotor case and develop a whole CFD methodology. Next, we develop a similar methodology for isolated phantom rotor cases and quadcopter cases based on the knowledge gained through CT rotor.

In solving the rotor flows we are employing overset mesh which forms the Near Body (NB) grids and moves along with the rotor blades. As rotor flows involve rotation coupled flow model is used in solving the mass and momentum equations. Coupled flow model solves the system of equations in a coupled manner using pseudo-time marching approach. The advantage of this method is its robustness for solving flows with dominant source terms like rotation, heat sources. This is what we exactly require in our case which involves a range of rotational speeds. Roe FDS scheme is used for computing inviscid fluxes in the domain. As we are also interested in observing the vortex shedding and computing wake of the rotor flows implicit unsteady approach seems a better time integration scheme. For an explicit unsteady scheme, CFL number determines the same physical time step for all the cells in the domain. This approach is generally not suited for incompressible flow simulations. As we are working in a flow regime with a maximum Mach number of 0.43 implicit unsteady approach seems a reasonable choice.

In the implicit unsteady approach, each physical time step is divided into a set of inner iterations for the solution to converge for that time step. Study

is performed initially to determine the number of inner iterations required for solving rotor flows. Inner iterations of 10, 15, 20 are tested out and a decision of using 15 inner iterations is reached. Many quantities like residuals of continuity, momentum, etc are observed for these tests and 15 seems a good enough number during which convergence is obtained for that particular time step. For most of the simulations in this thesis, 15 inner iterations are used unless otherwise specified. Pseudo time stepping is used in these inner iterations which is dependent on the Courant number used for the simulation. For implicit unsteady approach, an optimal balance of inner iterations and physical time step needs to be approached for the desired accuracy in time. A constant Courant number of 30 is used from hereon.

4.1 Caradonna and Tung rotor

In chapter 2 we have discussed uncertainity in some of the geometrical parameters of the Caradonna and Tung rotor. Rotor root cut radius is assumed to be 0.25 R and the blade geometry is made with NACA 0012 profile without any camber or twist in SOLIDWORKS. The rotor radius is offset of about 0.25 C from the center of the blade in the chordwise direction. The blade dimensions and other details are mentioned in table 4.1 below. Rotor hub geometry is omitted from this study as has been done by many other studies[3,24].

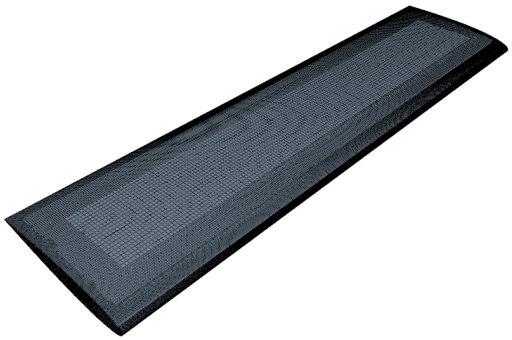

Figure 4.1: Surface mesh of CT rotor blade

The process of discretizing the domains into smaller units is known as

Table 4.1: Caradonna and Tung rotor parameters

Parameter	**Metric**
Airfoil	NACA 0012
Number of blades	2
Rotor radius (m)	1.143
Blade Chord (m)	0.1905
Blade twist (°)	0

meshing. Meshing operation is the basic step that facilitates solving the discretized governing equations in the domain. The mesh generated needs to meet certain quality criteria in the areas of Aspect Ratio (AR), cell skewness angle, slivers, negative jacobians, etc. The presence of any distorted or bad quality cell results in an inaccurate solution and also causes transmission of this inaccuracy over the whole domain. Most of the commercial mesh generators do have quality checks and the mesh generated has to go through them for successful operation.

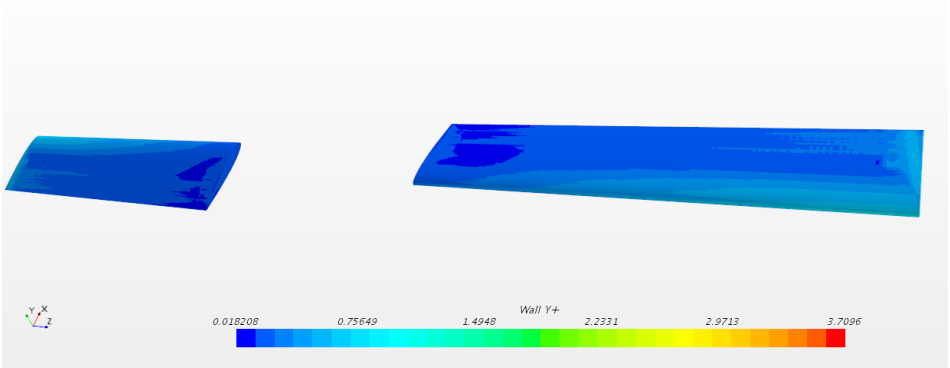

Figure 4.2: Scalar scene showing wall y+ for rotor blades

First, the rotor blade is surface wrapped to generate a better quality surface mesh. The surface wrapper is also used in the intent of its further use in quadcopter study. A better quality surface mesh also helps in the generation of better core mesh. To enhance the quality of the surface mesh, surface controls,

and curve controls are used. By using these, better control is obtained to perform curvature refinements and to keep the geometrical shape intact. Figure 4.1 shows the suface mesh of Caradonna and Tung rotor blade.

$$y^+ = \frac{\rho U L}{\mu} \tag{4.1}$$

Wall y^+ value is important to ensure that the boundary layer is properly resolved. For the rotor flows it is recommended to have a wall $y^+ < 1$. Prism layers are generated in such a way that wall $y^+ < 1$ is ensured for maximum cells. With the use of density (ρ), characteristic length(chord length for our flows), rotor RPM (which gives the tip speed), dynamic viscosity (μ) y^+ value is computed using equation 4.1. Figure 4.2 shows the wall y+ values for the rotor blades. In the below table 4.2 prism layer settings for different configurations is tabulated. where y_1 is the height of the first node from the wall, T is the thickness of the boundary layer.

Table 4.2: Prism layer settings for different configurations

Configuration	y_1 **(in mm)**	**No of layers**	**T (in mm)**
CT rotor	2.51e-3	10	0.4
Phantom rotor	5.93E-3	10	0.4
Quadcopter - rotor surfaces	5.93E-3	10	0.4
Quadcopter - fuselage surfaces	5.93E-3	5	0.4

Our rotor configuration is in hover and we would like to have a domain that would represent this. The domain size should be selected in such a way that it does not have any impact on the results. From reviewing the literature by Zhou, C., [25] and also using different domain sizes a cylindrical wind tunnel is created such that the top boundary is about 10 R distance and the bottom boundary is about 20 R from the rotor hub. The radius of the domain is taken

as 15 R.

4.1.1 Near Field Modeling

Near field region is the region in the immediate vicinity of rotor blades. The mesh setup in this region needs to be of adequate resolution to allow the generation, conservation, and convection of vortices shed. The baseline case used for this study made use of cylindrical volume sources for refinement. Near field study conducted shows that these volume sources are inadequate and require a further increase in the refinement zones and sizes. To improve the predictions the practice of using inflated bodies as volume refinements started.

Table 4.3: Dimensions of near wake refinement zones

Refinement zone	**BL (in mm)**	**M1**	**M2**	**M3**	**M4**
VC1	0.1	0.05	0.1	0.1	0.15
VC2	0.2	0.1	0.1	0.2	0.3
VC3	0.4	0.2	0.2	0.4	0.6
VC4	-	0.4	0.4	0.8	1.2

The study involving the results of a systematic increase in sizes of these refinements will be discussed in the following chapter. In table 4.3 we can see the sizes of different refinement zones with respect to the chord length. BL is the baseline case with only three cylindrical volume sources. Use of 4^{th} refinement zone is implemented from cases M1 to M4. In this table, VC1 represents the volume source that is closest to the blade wall and gradually moves away from it as we reach VC4. Figure 4.3 shows a closer look at the mesh scenes of different schemes and the effect of the refinement zones.

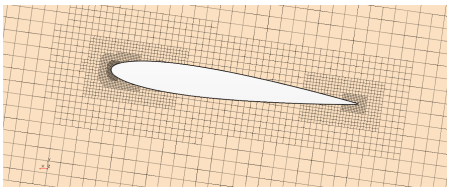

(a) Base line(BL) case

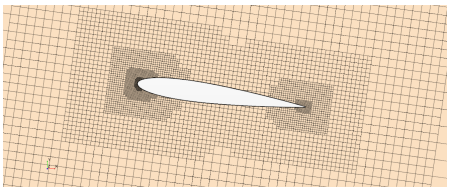

(b) M2 case

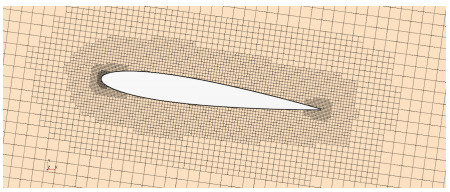

(a) M3 case

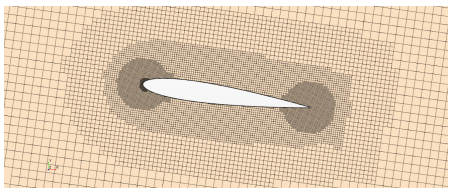

(b) M4 case

Figure 4.3: Near field mesh scenes of various meshing schemes

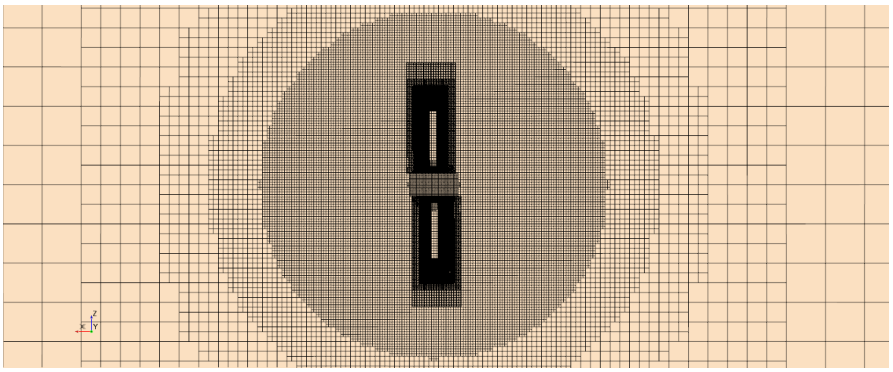

Figure 4.4 Far field mesh scenes of CT at Y=0

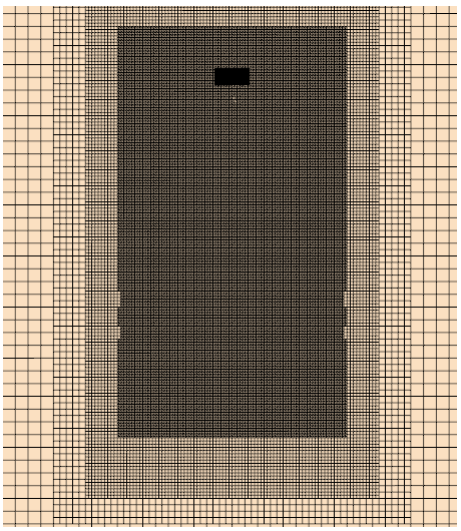

Figure 4.5 Far field mesh scenes of CT rotor at X=0

4.1.2 Far Field Modeling

The rotor wakes being generated now need to convect into the downstream and diffuse. This diffusion should be due to the inherent diffusive property of turbulence but not be propelled due to the insufficient grid resolution. Insuf-

ficient grid resolution results in artificial rotor wake diffusion which results in inaccurate values. The impact of these far wake grids on the results is also studied. Three initial configurations with far wake grids stretching 2.5 R, 7.5 R, and 15 R downstream is considered. A special case (M4-B) with a modification only in the wake grid resolution is also evaluated.

4.2 Isolated Phantom rotor

Caradonna and Tung rotor studies provide us with a good understanding of the modeling of rotors in hover. In the next chapter, the results discussed provides us with the best possible meshing strategies for both near field and far field regions. In the CT rotor all the refinement zones, domain sizes and mesh sizes used are either based of off the chord length or rotor radius. This makes it easy for defining these zones and also the base mesh sizes for this case. Direct application of best meshing strategy for the near field of CT rotor results in mesh size of about 110 million cells. To avoid this scenario the volume sources are tweaked a bit to reduce this computational size. Two meshing strategies(P1 and P2) are considered for this case at three different RPM levels.

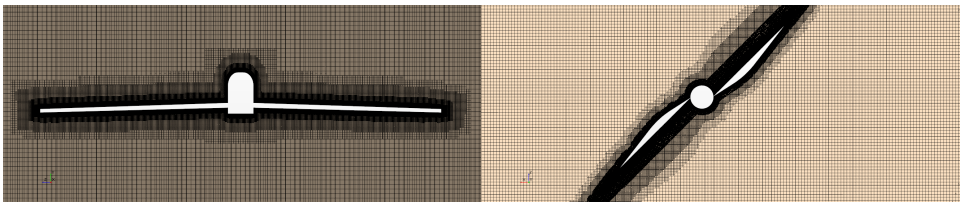

(a) (b)

Figure 4.6: Mesh representation of the isolated phantom rotor at (a) X =0 (b) Y = 0

4.3 DJI Phantom 3 quadcopter

The rotor part is the main area of concern for modeling a quadcopter in hover. Tackling the isolated configuration of the phantom rotor has given us an idea on how to proceed for meshing of a quadcopter. Quadcopter geometry is preprocessed using Hypermesh to make it suitable for CFD simulation.

Patching of open rotor zones, separation of the rotor from the fuselage body is accomplished in Hypermesh. Quadcopter rotors, fuselage are all individually wrapped which would ease the process of creating mesh zones as seen in the figure 4.7.

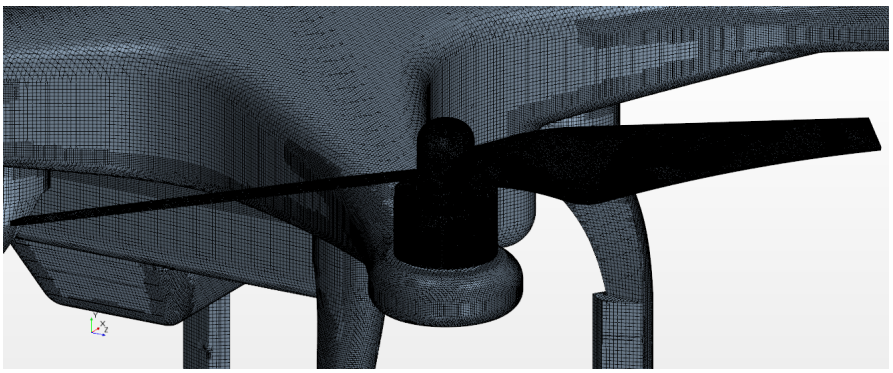

Figure 4.7 Surface mesh scene of rotor and fuselage

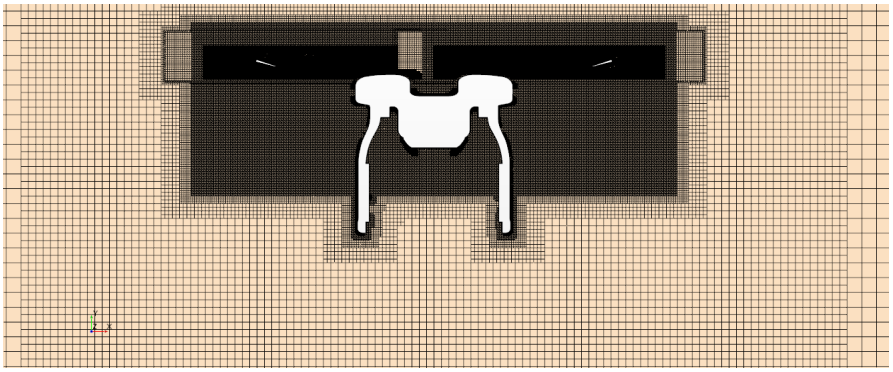

Figure 4.8 Mesh slice of Fuselage and rotor on a plane parallel to Z = 0

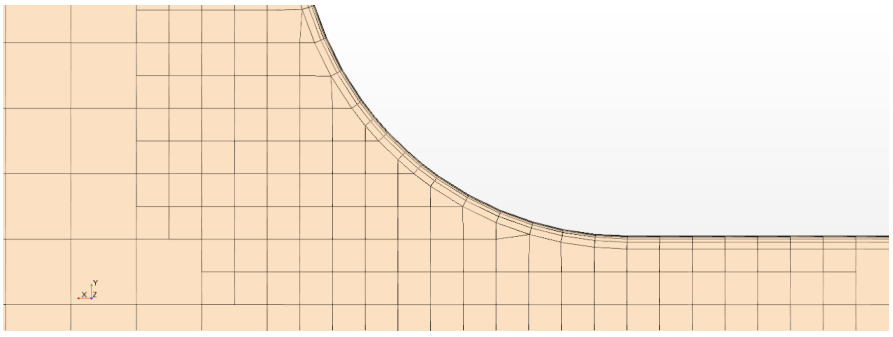

Figure 4.9 Mesh slice of prism layers on fuselage on a plane parallel to Z = 0

Quadcopter fuselage although present near the rotor systems do not have any rotating components of its own, so to reduce the computational size the

number of prism layers is reduced to 5. Figure 4.9 shows a zoomed in view of the fuselage with only 5 prism layers. Rotor region and its wake are resolved like in the previous cases ignoring the presence of fuselage in its vicinity. Fuselage and its surrounding regions in wake of the rotor are ensured to have sufficient resolution. An inflated body of fuselage is used for this purpose. Interfaces are created for different rotor regions and also rotor and background regions.

CHAPTER 5: RESULTS & DISCUSSIONS

5.1 Caradonna and Tung rotor

5.1.1 Mesh Independence Studies

The mesh independence study is performed for CFD simulations to decide on the mesh size to be implemented. Mesh size is gradually decreased and aerodynamic coefficients are computed for these cases. Deciding on mesh size and corresponding accuracy is always a trade off and requires good decision making. For hovering rotor applications optimum mesh size needs to be decided for both near wake and far wake regions. Base mesh size that is used for hover studies is taken as a fraction of rotor blade chord length. Most of the studies start with a base mesh size of 0.2 C for the far wake region [29,31]. This value is first chosen for starting mesh independency studies in this thesis.

5.1.2 Near Wake Modeling

Core mesh in the vicinity of rotor blade regions needs to be of adequate resolution for vortex generation and convection. This present section explores the impact of volumetric refinements in this area on the hover performance characteristics. Cylindrical volumetric refinements used in the baseline case has shown to have an error of about 5.32% with the experimental data as shown in table 5.1. M3 case with an increase of about 2.3 million cells has shown to improve the prediction by about 0.72% which is a reasonable improvement. M4 case here shows the best prediction with an error of only about 4.06%. The reason for improvements can be attributed to the increase in refinement zone's size. With this increase in size, the whole of the near wake region which these zones encompass is provided with a better resolution. Table 5.1 compares the computed thrust coefficient with the experimental values available. Torque coefficient and FM values are also provided in the table. Studies conducted on CT rotor do not have experimental values for these. M1 case which uses

Table 5.1: Hover performance characteristics of various mesh schemes

Mesh scheme	$\mathbf{C_T}(^*10^{-3})$	**% error**	$\mathbf{C_Q}(^*10^{-4})$	**FM**
BL	4.845	5.33	4.48	0.532
M1	4.846	5.35	4.49	0.532
M2	4.822	4.82	4.45	0.532
M3	4.812	4.61	4.48	0.527
M4	4.787	4.06	4.46	0.525

inflated bodies instead of cylindrical zones has almost the same predictions as the baseline case. This indicates that the refinements at the leading edge, trailing edge and tip regions are of significant importance. Refinement at the inner sections of the blade does not impact the results of integrated quantities or even sectional pressure coefficients. FM and C_Q values are only slightly impacted by these improvements. Figure 5.2 shows the plot of torque convergence history and figure 5.3 shows FM convergence history. M2 case has the lowest torque coefficient value and this results in a higher FM value. FM value predicted for the M2 case is almost equal to that of BL and M1 schemes. FM values for different schemes BL-M4 show little sensitivity to near wake grid resolution. This is in accordance with Hariharan, N., et al [22] which also indicates that FM has little sensitivity to the rotor wake grid beyond certain mesh resolution.

The rotor simulations are all started from quiescent flow conditions, i.e from rest conditions. It is estimated that about 20 rotor revolutions are required for the initial disturbance to be convected out of the flow domain[26]. Simulations for this section are run for a total of 30 revolutions, the first 20 revolutions are required for the purpose of convecting the starting vortex out. The simulations are run for 10 more revolutions to observe the convergence of hover performance parameters. It is observed from the results of these param-

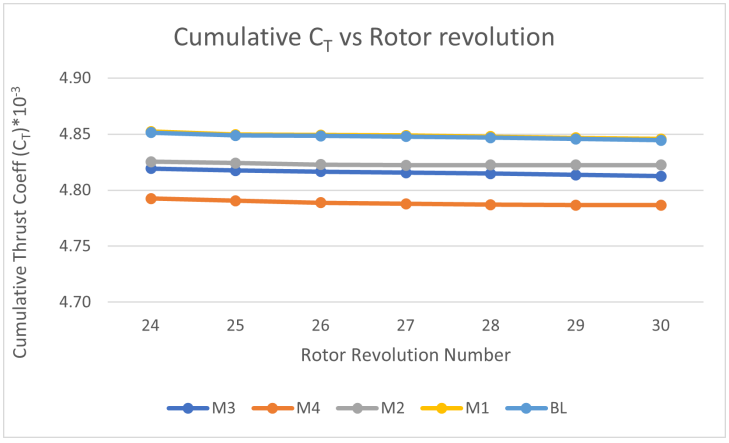

Figure 5.1: Plot of thrust convergence history versus rotor revolution number.

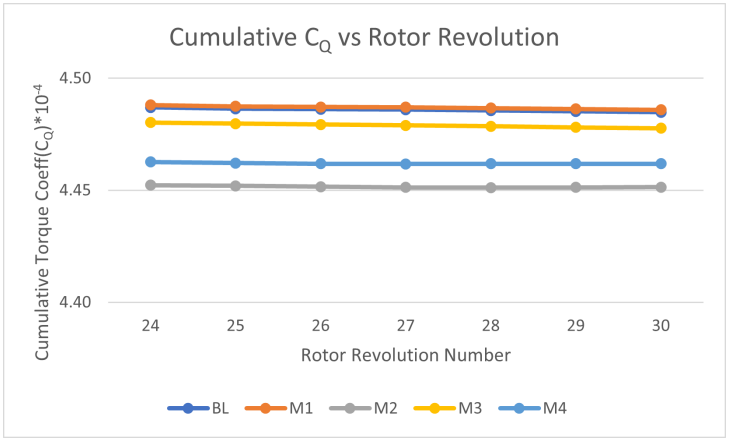

Figure 5.2: Plot of torque convergence history versus rotor revolution number.

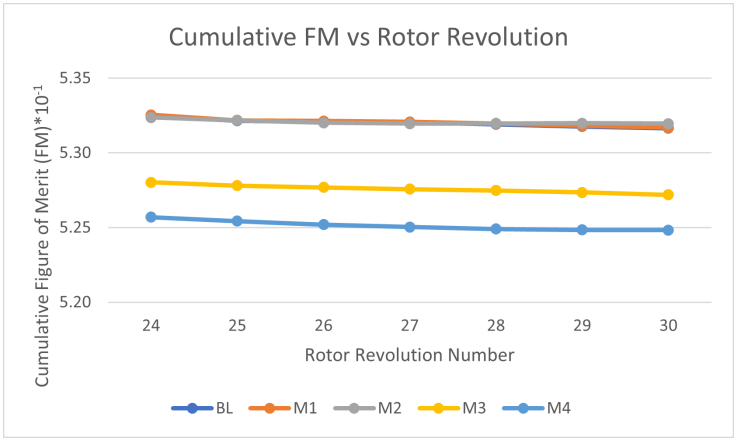

Figure 5.3: Plot of FM convergence history versus rotor revolution number.

eters that they have not reached perfect convergence until 24 revolutions and exhibit small fluctuations. This can be concluded to be due to the presence of initial disturbance. Figure 5.1 shows the convergence history of cumulative rotor thrust coefficient versus rotor revolution number. Here rotor thrust coefficient is cumulatively averaged starting from 24^{th} rotor revolution till the 30^{th}.

Observing the results for these BL - M4 simulations there has been an increment in the prediction of thrust coefficient by only 1.3% which is not very significant in an engineering perspective. Observation of the wake resulted from these simulations it is noted that M4 represents a fully developed wake structure better than the BL, M1, M2 schemes. It is further left to the discretion of readers here to choose the appropriate mesh scheme based on their application. For a system where the wake of rotors needs to be accurately modeled, it is recommended by the author to use the M4 scheme. The necessity of accurate modeling of rotor wake is made clear in the results of quadcopter where the interactions of the rotor - rotor wake is a detrimental factor. For other applications where the requirement is only computing thrust, torque, and pressure coefficients other schemes can be used and save a lot of computational resources and time.

These computations were performed on UNCC HPC Cluster ORION using 48 cores for BL - M3 simulations. BL, M1, M2 required a total computational time of about 96 - 110 hours (4-5 days). M4 simulation used 96 cores and required a total time of 168 - 180 hours (7-8 days). The computational time is also a judging criterion to select an appropriate scheme.

5.1.3 Turbulence modeling

S., Yoon [28] states that the RANS model fails to predict FM accurately in most of the scenarios. This discrepancy increases in the presence of strong blade vortex interactions (BVI). No specific RANS turbulence model can be favored for the prediction of aerodynamic coefficients. All the turbulence models demonstrate little to no differences. Surface pressure coefficients plot below in the figure 5.4 reassure the same thing except for small indistinctive differnces. These differences are keenly observed and distinguished for different models. From the figures as we move towards the outboard station of the wing, the computed sectional pressure coefficient values fall exactly onto the experimen-

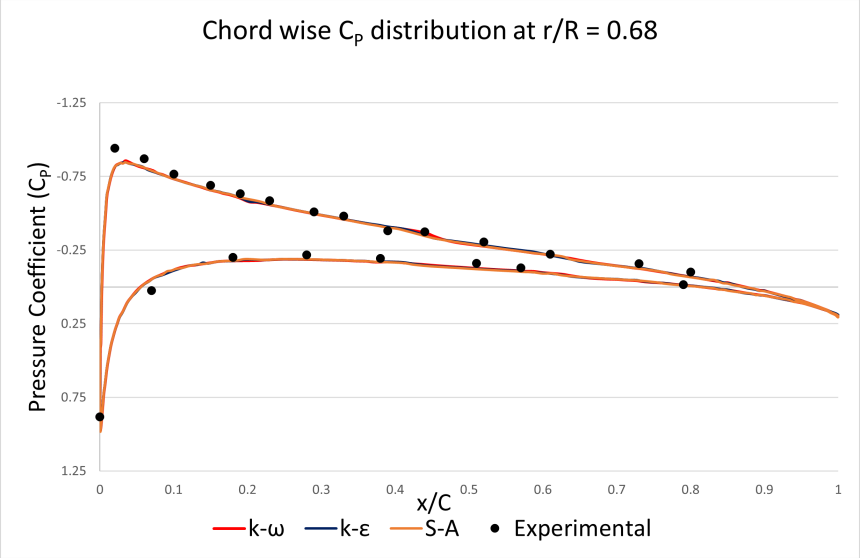

Figure 5.4: Plot of chordwise surface pressure coefficient(C_P) at a radial location of r/R = 0.68.

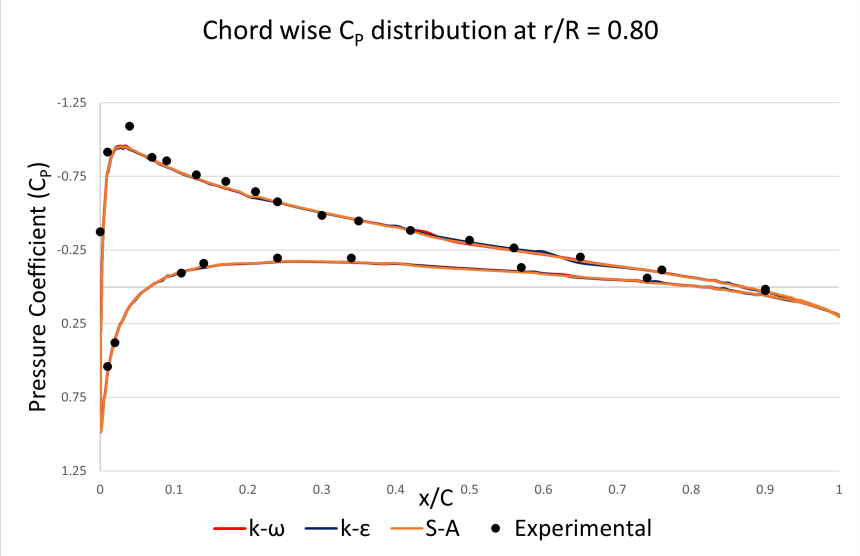

Figure 5.5: Plot of chordwise surface pressure coefficient(C_P) at a radial location of r/R = 0.80.

tal values.

From the figures 5.4, 5.5 & 5.6 it can be observed that as we move towards the outboard radial locations the computed pressure coefficient values fall on to the experimental results. In the figure 5.4, 5.5 the negative pressure peak is underpredicted by the computations and it is similar for all the turbulence models. The negative peak pressure value is higher at the radial location of r/R=0.96 when compared to values at r/R=0.80,0.69. This also ascertains the fact that the maximum amount of thrust is produced at the outboard loca-

tions. The upper surface of the rotor blade has a negative pressure value while the lower surface maintains a positive value.

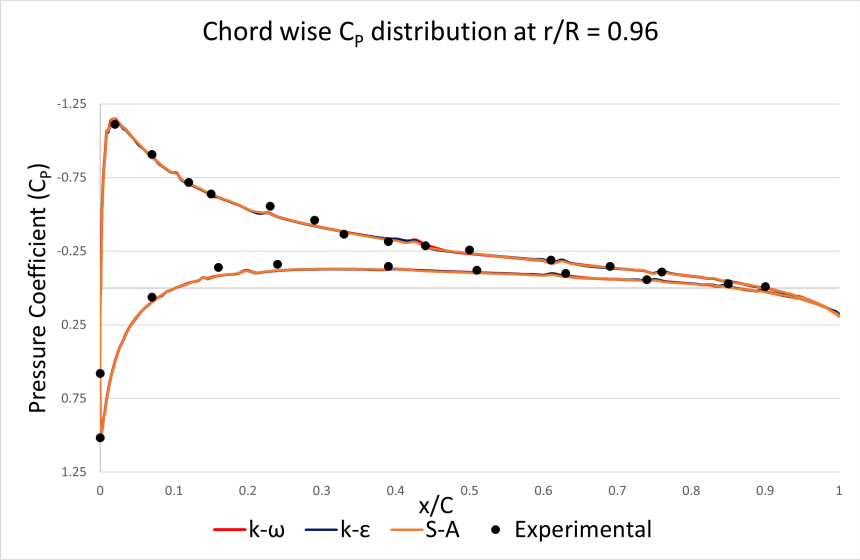

Figure 5.6: Plot of chordwise surface pressure coefficient(C_P) at a radial location of r/R = 0.96.

5.1.4 Mesh Independency study

In this section, we discuss the mesh independence study carried out for rotor hover studies. M4 case which we observe to predict the best is selected for this study. The base size which was 0.2 times the chord length is varied by 20%. Ideally, a factor of 2 should be used for grid independency studies but halving the base size would increase the computational size by a large extent and would no longer be computationally feasible. Table 5.2 presents the thrust coefficient for cases MI 1, MI 2, MI 3. MI 1 case with a 20% increase in the base mesh size shows an increase in predicted thrust value and a variation of about 1.3%. MI 1 scheme took about 72 hours to complete on 36 cores whereas MI 2 required about 144 hours on 48 cores. MI 3 which has a lower base used 96 cores for simulation and almost 240 hours.

Figure 5.7 shows iso-surface of Q-criterion colored with pressure coefficient on Y =0 plane for MI 1-3 schemes. The figure for MI 1 scheme indicates

Table 5.2: Variation of C_T with the mesh size.

Mesh scheme	**Base Mesh Size (m)**	**C_T**$(*10^{-3})$	**% error**
MI 1	0.04572	4.789	4.13
MI 2	0.0381	4.724	2.69
MI 3	0.03048	4.738	3

(a) MI 1

(b) MI 2

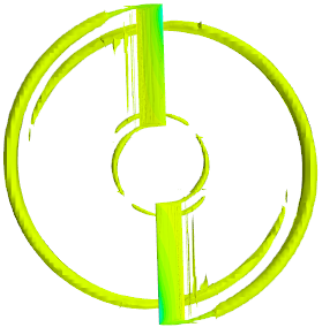

(c) MI 3

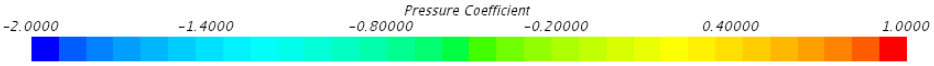

Figure 5.7: Root vortices of Caradonna and Tung rotor on a plane Y = 0 (a) MI 1 scheme indicating smeared root vortices for Q-criterion = $8500/s^2$ (b) MI 2 scheme for Q-criterion = $9000/s^2$ (c) MI 3 scheme for Q-criterion = $11000/s^2$

that the resolution at the rotor root regions is insufficient for the formation of distinct root vortices. Contrary to the general observation which indicates downstream convection of root vortices we can observe the root vortices to be convecting upstream. This can be seen in the figure 5.8 where the root vortices

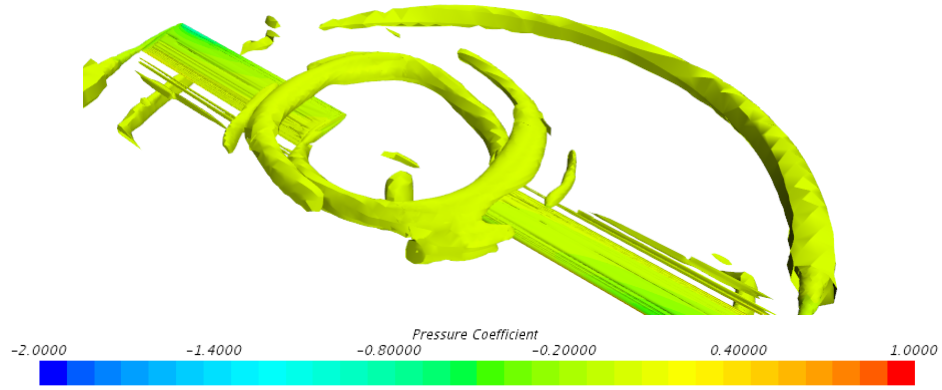

Figure 5.8: Zoomed in view of root vortices of Caradonna and Tung rotor for iso-surfaces with Q-criterion = 8500/s^2.

are convecting in the opposite direction of tip vortices. MI 1 scheme is observed to conserve the tip vortex for a very short wake age of about 160 degrees by visual inspection. MI 2 and MI 3 schemes both have sufficient resolution to allow formation and convection of distinct root vortices. MI 3 scheme preserves for a longer wake age than the MI 2 scheme even though only for a small wake age difference of about 15-30^o. MI 3 scheme uses 34 million cells whereas MI 2 case uses about 18 million cells which clearly indicates that the computational effort is not worth it. In the further section where we explore the aspect of far field modeling further improvements are made in this area.

5.1.5 Far Field Modeling

In the earlier sections, we have discussed in detail the meshing schemes undertaken for modeling the near field region of the rotor blade. The wake grid that has been employed till now used a grid size of 0.2 C which was adequate for the prediction of hover parameters. Deciding on the far wake grid is first carried out. Far field grid with sizes of 2.5 R, 7.5 R, 15 R in downstream direction is tested. The simulation with 2.5 R wake grid size is found to be inadequate for preserving the vortex structures for rotor applications. Grid sizes with 7.5 R and 15 R showed no differences and 7.5 R is used for further simulations. This wake grid had a resolution of 0.2 C and a special case with a

resolution of 0.1 C is also evaluated. Computational effort for these simulations required the same time as required for MI 4 case.

Figure 5.9 shows the comparison of iso-surfaces of M4 case with the special

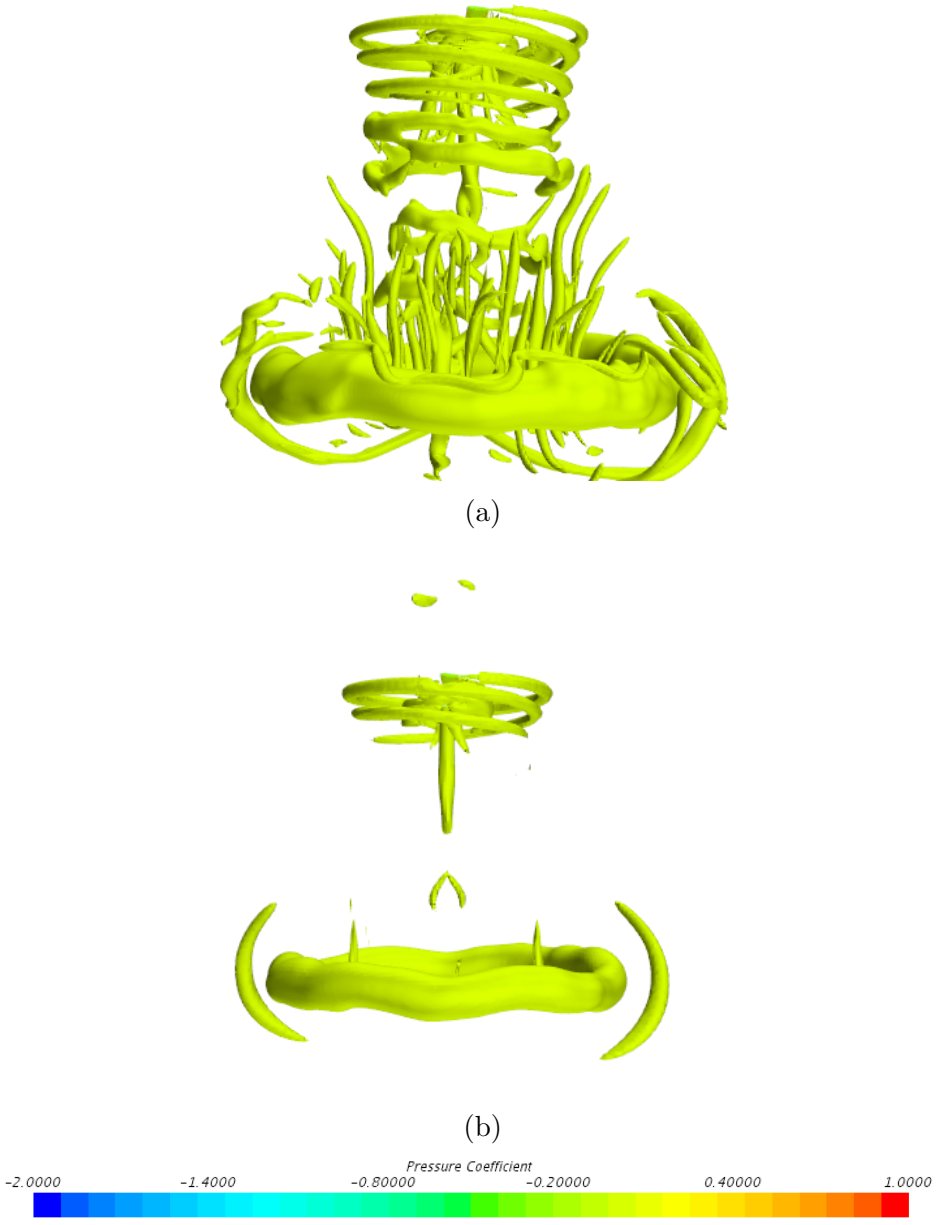

Figure 5.9: Lateral view of vortex wake for Caradonna and Tung rotor represented by iso-surfaces of Q-criterion = $1000/s^2$ for different mesh schemes on a plane parallel to Z = 0. (a) M4-B scheme (b) M4 scheme.

case M4-B whose only difference is the use of 0.1 C mesh size in the wake grid. We can observe from the figure that the M4 scheme (b) is inadequate to preserve the vortex structures in the far wake region. The vortex structures disintegrate beyond a point in the case of M4 scheme and breaking of

vortex structures occur. Further refinement studies can be performed in this far wake region for better understanding and obtaining mesh independency. Based on the results obtained it can be assessed that the grid is sufficiently fine to convect the vortices in the far wake. Further refinement here is deemed unnecessary and not pursued in this study. The other issue is an excessive computational requirement for using a further fine grid in the far wake.

Figure 5.10 shows the vortex sheet formation along with tip and root vor-

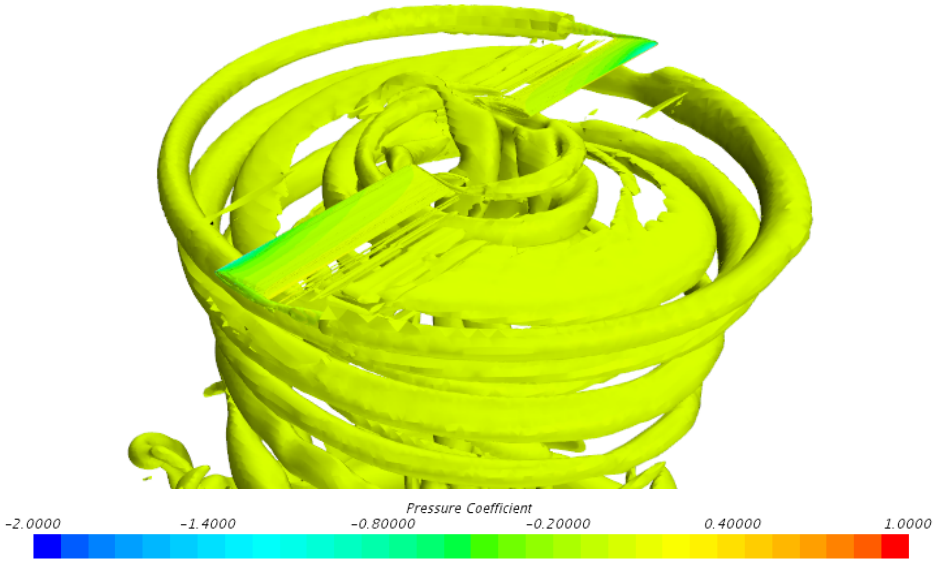

Figure 5.10: Isometric view of vortex sheet of M4-B scheme for Caradonna and Tung rotor

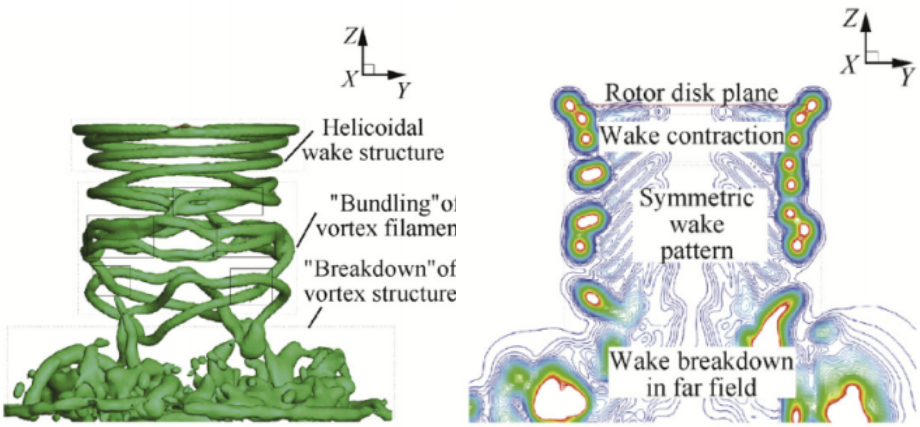

(a) (b)

Figure 5.11: Wake structure for the Caradonna and Tung rotor in hover [24] (a) Lateral view of isosurface (b) Vorticity contour over a vertical plane [24].

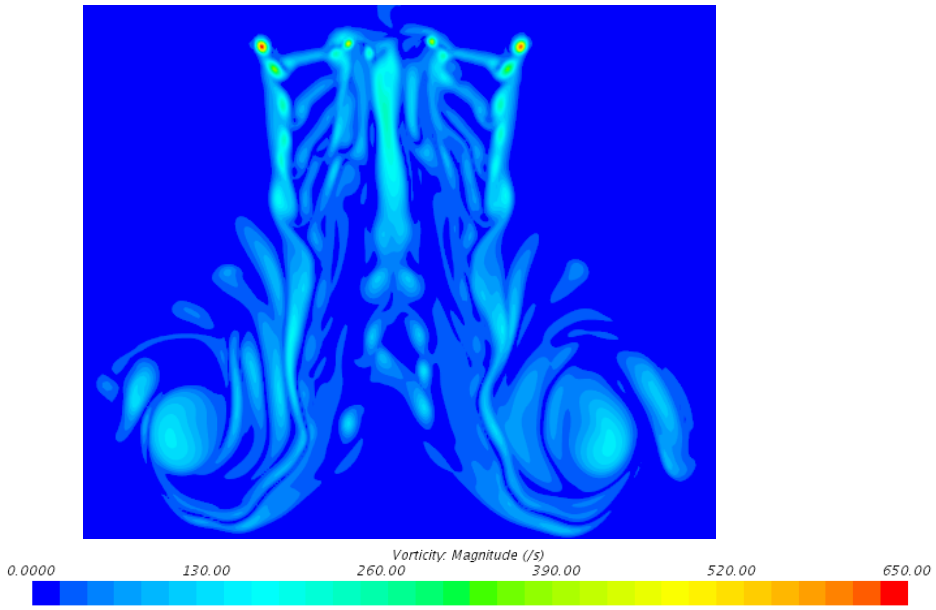

Figure 5.12: Vorticity magnitude scene of M4-B scheme on a plane parallel to Z = 0 at the center of the hub.

tex structures. Vortex sheet is observed to convect faster into the downstream than the tip vortices which is consistent with the observations of R., Strawn [6]. Figure 5.9 (a) also shows a fully formed vortex wake behind a rotor blade. Here vortex structures in the near wake and far wake can be clearly identified and distinguished. This can be compared to the figure 5.11 (b) which explains the whole structure of wake behind a rotor. As seen in the results we could see the helical wake structure in the immediate vicinity of the rotor. These helical structures then bundle together in the far wake region and finally breakdown. A comparable wake structure is obtained for Caradonna and tung rotor with W., Liangquan [24]. Rotor wake contracts below the rotor plane as can be seen in the figure 5.11 (b). The vorticity contour shows a decrease in the radius of the helical structure immediately below the rotor plane and that is rotor wake contraction. Figure 5.12 shows a similar wake contraction below the rotor disk plane. The helical structure of the vortices is maintained for some revolutions and as they move into the far wake these begin to bundle together. This bundling phenomenon is known as "vortex pairing instability". This leads to the breakdown of the vortex structures in the far wake region. Figure 5.12 also

shows asymmetry in the vortex structure of the far wake. This asymmetry is introduced due to shear force at the edge of vortex-induced downwash.

5.1.6 Time step Independency study

The time required for obtaining convergence for rotor applications is very high and generally requires over 10 revolutions. So the choice of appropriate time step becomes predominant. In this study, three cases DT 1, DT 2, and DT3 with time steps of 0.5^o,1.0^o, and 1.5^o are used. While using a time step of 1.5^o with similar settings the solver was not able to converge due to courant number related convergence issue in the simulation. Earlier in the numerical setup, we learned that in implicit unsteady solver courant number is related to the inner time steps and also an optimal balance of the time step and inner iterations is required. This led to increasing the inner iterations to 20 for the case of DT 3 keeping the rest of the parameters same. As inner iterations are increased this would also increase the computational time. DT 3 on a whole would require less computational time than its counterparts.

Table 5.3: Variation of hover performance parameters with time step.

Mesh scheme	$\mathbf{C_T}(^*10^{-3})$	$\mathbf{C_Q}(^*10^{-4})$	**FM**
DT 1	4.710	4.43	0.516
DT 2	4.705	4.42	0.516
DT 3	4.706	4.42	0.517

The computational time required for DT 3 scheme with a time step of 0.5 degrees is twice that of DT 2 scheme and required more than 2 weeks on 48 cores. This scheme is highly not recommended by the author and would strongly suggest starting with the use of 1 degree or more. DT 1 takes the shortest time of all with only about 2 - 3 days.

Table 5.3 shows little to no variations in the hover performance predictions

and also the wake observed through iso surfaces shows no significant differences. From now on the studies involving CT rotor can employ 1.5^o as the time step and also further research can be done by incrementing the time step by a small amount of 0.5^o to a time step of 2.0^o.

5.2 Isolated Phantom rotor

Schemes used for Caradonna and Tung rotor have been validated to be sufficient for hover performance prediction. These schemes are tweaked and applied for the case of the DJI phantom 3 rotors. The isolated rotor of the DJI Phantom 3 is studied and its hover performance is assessed in this section. Two meshing schemes P1 and P2 are used for assessing. S-A turbulence model which is known to be better for assessing aerodynamics of an airfoil is used along with $k-\omega$ SST model for RANS turbulence modeling.

Initial simulations for 3600 RPM have been performed for isolated phantom rotor using S-A and $k-\omega$ SST model. The thrust coefficient plots obtained for these simulations showed that the $k-\omega$ SST model had higher fluctuations whereas S-A model had a smooth and periodic result. In table 5.5 thrust coefficient value for 3600 RPM $k-\omega$ SST model has shown a higher deviation of about 28% which is quite high. Both schemes P1 and P2 show similar deviations from the experimental value. S-A model used for 3600 RPM case has made a better prediction with an error of only 13% and in general, it is observed that the S-A model has shown better predictions. This reason prompted the author to utilize the S-A turbulence model for RPM ramp cases. P1 and P2 have predicted the same for S-A case at the RPM level of 3600. With the increase in RPM to 5400 and 7200 P1 cases are observed to perform better and this case is considered for quadcopter applications.

Results obtained for thrust showed a definite trend for both the schemes but there is no such trend in the case of thrust coefficients as seen in table 5.5. The error for thrust for the P1 scheme is observed to be decreasing with an

Table 5.4: Thrust predictions of isolated phantom rotor.

RPM	**Expt.**	**SST P1**		**S-A P1**		**SST P2**		**S-A P2**	
		Values	**Error**	**Values**	**Error**	**Values**	**Error**	**Values**	**Error**
3600	0.93	1.19	28	1.05	12.9	1.19	28	1.05	12.9
5400	2.22	-	-	2.32	04.5	-	-	2.45	10.4
7200	3.98	-	-	4.11	03.3	-	-	4.25	6.8

Table 5.5: Thrust coefficient(1e-2) predictions for isolated phantom rotor.

RPM	**Expt.**	**SST P1**		**S-A P1**		**SST P2**		**S-A P2**	
		Values	**Error**	**Values**	**Error**	**Values**	**Error**	**Values**	**Error**
3600	8.90	10.5	28	9.28	4.3	10.5	28	9.29	4.4
5400	9.20	-	-	9.10	1.1	-	-	9.60	4.3
7200	9.25	-	-	9.05	2.2	-	-	9.37	1.3

increase in RPM. A similar trend is also observed for P2 scheme but still it has higher error than the P1 scheme. Over prediction of thrust results for $k-\omega$ SST model also translates into overprediction for thrust coefficient results by quite a margin. Studies performed in N., S., Zawodny [9] used a DES model for performance predictions while URANS has been implemented in our studies. Also a time step of 0.25° for simulating the isolated phantom rotor. Use of this time step is unfeasible as it increases computational time twelvefold as a time step of 2.5° in this study. Although it has been noted in our research of Caradonna and Tung rotor that the impact of timestep is not significant. So the higher error for the isolated phantom rotor case can be attributed to the inability to accurately model the wake region.

5.3 DJI Phantom 3

In this section computed results are discussed for DJI Phantom 3 quadcopter. Here we focus on the effects of the aerodynamic interactions between rotors and also between rotor and fuselage. The aerodynamic behavior of a

Table 5.6: Comparison of Turbulence models for performance predictions.

	Expt.	**IDDES**		**IDDES(refined)**		**URANS**	
		Values	**Error**	**Values**	**Error**	**Values**	**Error**
Thrust(lbf)	1.24	1.07	14	1.1	11	1.0	19
Thrust coeff(1e-2)	1.32	1.05	20	1.06	19	0.96	27

quadcopter rotor is entirely different from that of an isolated rotor. Quadcopter rotor is in the presence of fuselage which acts as a wall structure. The rotor wakes of the quadcopter rotor interacts with the wake of other rotors and is found to be influencing its performance.

In table 5.6 we could observe the predictions made by IDDES and URANS models. IDDES refined is a case with a 10% decrease in the base mesh size to observe the effects of mesh refinement. IDDES model is observed to predict better value of thrust and thrust coefficient. Unrefined IDDES model underpredicts the thrust value at 1.07 lbf with an error of 14% compared to the experimental value. This prediction has been bettered with using IDDES refined case which has an error of only 11%. URANS model which comprises about 230 million volume cells is found to underpredict thrust values whereas IDDES models with only 38 million cells and 50 million cells have a very good prediction. For the first couple of rotations, a time step of 1^{o} with only 1 inner iteration is used. This is implemented to speed up the process of initialization and to reduce computational time. After two rotations the inner iterations are increased to 10 and the simulation is continued. The use of 10 inner iterations enables convergence for that time step. URANS model which was earlier found to be adequate for predicting isolated rotor performance is now unable to predict the quadcopter performance. This raises concern regarding the ability of URANS in predicting complex rotor-rotor and rotor-fuselage interactions. These simulations have been estimated to take around 100 hours although the exact time is not noted for these. The use of a time step of 2.5 deg has facilitated the faster completion of these simulations. P1 scheme is estimated to

Table 5.7: Performance of Individual components of DJI Phantom 3

	IDDES	**IDDES(refined)**	**URANS**
Rotor(lbf)	1.20	1.22	1.10
Fuselage(lbf)	-0.13	-0.12	-0.13
Quadcopter(lbf)	1.07	1.10	0.97

take about 120- 144 hours to complete as it has higher volume cells than P2 scheme.

Table 5.7 indicates the individual performance of different components of the quadcopter. Collective rotor performance is evaluated for all the models. As noticed earlier that the URANS model is underpredicting thrust, this is due to the underprediction of collective rotor thrust. IDDES models predict thrust with a relative change of about 10% with respect to URANS model. Individual rotors are all equally contributing to the collective rotor performance for all the models. The geometry of DJI Phantom 3 which is almost symmetrical also validates this. Fuselage download is the same for every case which indicates similar flow field predictions near the fuselage for URANS and IDDES models. Rotor-fuselage interactions which can be quantified in the form of fuselage download are same for all three cases. This implies that URANS model is predicting rotor-fuselage interactions with reasonable accuracy.

Table 5.8: Thrust comparison for Isolated rotor and quadcopter configurations.

	Isolated Rotor	**IDDES***	**IDDES(refined)***	**URANS***
Thrust(lbf)	0.24	1.28	1.29	1.16

In the table 5.8 collective rotor performance is compared to the isolated DJI Phantom 3 rotor performance. To enable this comparison the collective rotor performance is normalized by four times the performance of the isolated

rotor. The asterisk used here indicates the use of this normalized averaged thrust value. All the models show increased rotor performance. This can be reasoned to the presence of fuselage. This acts as a wall that increases the rotor performance and agrees with the results of [10,12]. OVERFLOW solver is used by the [20,29,31] to compute rotor flows. In these studies, a central difference algorithm is employed with 4^{th}-order accurate spatial differencing scheme. Low Mach number preconditioning is also used for inner iterations in an attempt to speed up the convergence. StarCCM+ commercial code used in this study has the ability to use only 2^{nd} order accurate spatial schemes. The results obtained here by StarCCM+ is comparable to the results obtained through the use of OVERFLOW. URANS simulations took almost 2 weeks to complete on 576 cores for completion whereas IDDES simulations took only 148 hours to complete although it utilized different time step and inner iterations on 144 cores.

CHAPTER 6: CONCLUSIONS

This final chapter is a summary of the research and reiterates important observations and conclusions obtained. A successful investigation on the hover performance prediction of an isolated rotor system and a quadcopter configuration is completed. A high fidelity simulation scheme is established by first validating Caradonna and Tung rotor system. This scheme is then applied to an isolated rotor system of quadcopter and DJI Phantom 3 quadcopter and the results show the repeatability of this methodology. The optimum method is selected based on the observed results for several test cases. The current study showed the influence of different meshing schemes in the near wake and far wake regions for hover prediction. Major results are presented in their respective sections. Here, important observations, comments on overall prediction capabilities are summarized below.

- A general framework for the simulation of rotorcraft is established in this thesis. This methodology is applied and studied for a multi-rotor system of quadcopter DJI Phantom 3.
- Hover performance parameters like thrust coefficient, torque coefficient, figure of merit (FM) and surface pressure coefficients are computed and successfully validated against experimental data. A fully developed wake is also observed and compared in this research.
- Performance of DJI Phantom 3 quadcopter is also analyzed and validated against experimental data. URANS, IDDES models are used in this research and it has been observed that IDDES is better for thrust prediction. Aerodynamic loads of individual components like rotor, fuselage is also computed.
- Rotor-fuselage interactions are observed to be predicted the same by different models. Whereas the collective rotor thrust is underpredicted by URANS model. This implies the difference in the prediction of a rotor

- rotor interactions by these models.

- Collective rotor performance of quadcopter is observed to be higher than that of the isolated rotor performance for all the models. The presence of fuselage acts as a wall structure which results in this increased rotor performance.

These observations show that with the methodology developed in this thesis aerodynamic performance characteristics of isolated rotor and quadcopter can be computed. This framework can be utilized in the design process of a quadcopter and help us in eliminating the requirement of a physical prototype. The study also demonstrates the deficiencies of URANS modeling in resolving fully developed wake for quadcopter configuration. IDDES - SA models show promise in predicting hover performance for quadcopter. Further studies is required for studying the fully developed flow for a quadcopter and also for exact quanitfication of multi-rotor interactions. Prediction of these models for quadcopter configuration at various RPM levels also needs to be assessed.

REFERENCES

[1] N. S. Hariharan, T. A. Egolf, and L. N. Sankar, "Simulation of rotor in hover: Current state, challenges and standardized evaluation," in *52nd Aerospace Sciences Meeting*, p. 0041, 2014.

[2] N. Hall, *Winglets*, National Aeronautics and Space Administration, May. 05, 2015. [Online]. Available:https://www.grc.nasa.gov/www/k-12/airplane/winglets.html

[3] P. Doerffer and O. Szulc, "Numerical simulation of model helicopter rotor in hover," *Task Quarterly*, vol. 12, no. 3, pp. 227-236, 2008.

[4] R. C. Strawn and M. J. Djomehri, "Computational modeling of hovering rotor and wake aerodynamics," *Journal of Aircraft*, vol. 39, no. 5, pp. 786-793, 2002.

[5] J. Ahmad and E. P. Duque, "Helicopter rotor blade computation in unsteady flows using moving overset grids," *Journal of Aircraft*, vol. 33, no. 1, pp. 54-60, 1996.

[6] R. Strawn and J. Ahmad, "Computational modeling of hovering rotors and wakes," in *38th Aerospace Sciences Meeting and Exhibit*, p. 110, 2000.

[7] F. X. Caradonna and C. Tung, "Experimental and analytical studies of a model helicopter rotor in hover," 1980.

[8] J. U. Ahmad and R. C. Strawn, "Hovering rotor and wake calculations with an overset-grid navier-stokes solver," in *AHS International Annual Forum*, 55 th, Montreal, Canada, pp. 1949-1959, 1999.

[9] N. S. Zawodny, D. D. Boyd Jr, and C. L. Burley, "Acoustic characterization and prediction of representative, small-scale rotary-wing unmanned aircraft system components," 2016.

[10] S. Yoon, P. V. Diaz, D. D. Boyd Jr, W. M. Chan, and C. R. Theodore, "Computational aerodynamic modeling of small quadcopter vehicles," in *American Helicopter Society (AHS) 73rd Annual Forum Fort Worth, Texas*, 2017.

[11] S. Yoon, H. C. Lee, and T. H. Pulliam, "Computational analysis of multi-rotor flows," in *54th AIAA aerospace sciences meeting*, p. 0812, 2016.

[12] P. Ventura Diaz and S. Yoon, "High fidelity computational aerodynamics of multi-rotor unmanned aerial vehicles," in *2018 AIAA Aerospace Sciences Meeting*, p. 1266, 2018.

[13] J. L. Pereira, *Hover and wind-tunnel testing of shrouded rotors for improved micro air vehicles design.* PhD thesis, University of Maryland, College Park, p. 349, 2008.

[14] C. Argyropoulos and N. Markatos, "Recent advances on the numerical modelling of turbulent flows," *Applied Mathematical Modelling,* vol. 39, no. 2, pp. 693-732, 2015.

[15] F. R. Menter, "Two-equation eddy-viscosity turbulence models for engineering applications, " *AIAA journal,* vol. 32, no. 8, pp. 1598-1605, 1994.

[16] B. E. Launder and D. B. Spalding, "The numerical computation of turbulent flows," in *Numerical prediction of flow, heat transfer, turbulence and combustion,* pp. 96-116, Elsevier, 1983.

[17] S. B. Pope, "Turbulent flows," 2001.

[18] P. Spalart and S. Allmaras, "A one-equation turbulence model for aerodynamic flows," in *30th aerospace sciences meeting and exhibit,* p. 439, 1992.

[19] D. C. Wilcox et al., "Reassessment of the scale-determining equation for advanced turbulence models," *AIAA journal,* vol. 26, no. 11, pp. 1299-1310, 1988.

[20] S. Yoon, T. H. Pulliam, and N. M. Chaderjian, "Simulations of xv-15 rotor ows in hover using over overflow," *Proceedings of the 50th AHS Aeromechanics Specialists, AHS, San Francisco, CA*, pp. 1-11, 2014.

[21] N. A. R. N. Mohd and G. N. Barakos, "Computational aerodynamics of hovering helicopter rotors," *Jurnal Mekanikal*, vol. 34, no. 1, 2012.

[22] N. Hariharan and L. Sankar, "A review of computational techniques for rotor wake modeling," in *38th Aerospace Sciences Meeting and Exhibit*, p. 114, 2000.

[23] H. Tennekes and J. L. Lumley, *A first course in turbulence.* MIT press, 2018.

[24] W. Liangquan, X. Guohua, and S. Yongjie, "High-resolution simulation for rotorcraft aerodynamics in hovering and vertical descending flight using a hybrid method," *Chinese Journal of Aeronautics*, vol. 31, no. 5, pp. 1053-1065, 2018.

[25] C. Zhou, *Assessment of tip planform effects on the hover characteristics of helicopter rotors.* PhD thesis, Georgia Institute of Technology, 2019.

[26] R. M. Eshcol, C. Zhou, J. Kim, L. N. Sankar, "A Comparative Study of Two Hover Prediction Methodologies." in *54th AIAA Aerospace Sciences Meeting,* p. 0300. 2016.

[27] C. R. Russell, J. Jung, G. Willink, and B. Glasner, "Wind tunnel and hover performance test results for multicopter UAS vehicles," 2016.

[28] S. Yoon, N. Chaderjian, T. H. Pulliam, T. Holst, "Effect of Turbulence modeling on Hovering Rotor Flows." in *45th AIAA Fluid Dynamics Conference,* p. 2766, 2015.

[29] P. G. Buning and T. H. Pulliam, "Near-body grid adaption for overset grids," in *46th AIAA Fluid Dynamics Conference*, p. 3326, 2016.

[30] L. A. Young, "Conceptual design aspects of three general sub-classes of multi-rotor configurations: distributed, modular, and heterogeneous," 2015.

[31] N. M. Chaderjian, "Navier-stokes simulation of UH-60A rotor/wake interaction using adaptive mesh refinement," 2017.